

CERIAS Tech Report 2000-26

**DIRECT SPACE-TO-TIME PULSE
SHAPING FOR ULTRAFAST
OPTICAL WAVEFORM GENERATION**

by Daniel E. Leaird

Center for Education and Research in
Information Assurance and Security,
Purdue University, West Lafayette, IN 47909

DIRECT SPACE-TO-TIME PULSE
SHAPING FOR ULTRAFAST OPTICAL
WAVEFORM GENERATION

A Thesis

Submitted to the Faculty

of

Purdue University

by

Daniel E. Leaird

In Partial Fulfillment of the
Requirements for the Degree

of

Doctor of Philosophy

December 2000

This thesis is dedicated to my family - Jennifer, my wife of thirteen years, our children Ian, Maclaine, and Aidan, and my parents Tom and Bobbie. This work is a testament to your loving support.

ACKNOWLEDGMENTS

The support, collaboration, and encouragement of Prof. Andrew Weiner has made this work possible. Without his counsel, I would have left this field long ago. To the students, past and present, post-docs, and visitors of the Ultrafast Optics & Optical Fiber Communications Laboratory, I have enjoyed our time together in the lab. These interactions remind me what it is that I love about this work.

The experimental optical pulse train generation devices investigated in chapter 4 would not have been possible without the design and fabrication expertise of A. Sugita, S. Kamei, M. Ishii, and K. Okamoto at NTT Photonics Laboratories. S. Shen, currently with Lucent Technologies (an alumni of the Ultrafast Optics & Optical Fiber Communications Laboratory), provided invaluable assistance in conducting the experimental studies of these devices. I thank IMRA America for the loan of the modelocked femtosecond erbium fiber laser that was used for part of these experiments.

TABLE OF CONTENTS

	Page
Acknowledgments	iii
Table of contents	iv
List of tables	vi
List of figures	vii
ABSTRACT	x
1. Introduction	1
2. Background	5
3. DST Bulk Optics Configuration.....	11
3.1 DST Pulse Shaper Description.....	14
3.1.1 Quantitative argument.....	14
3.1.2 Qualitative argument.....	17
3.2 Complete Apparatus.....	20
3.2.1 Measuring the space-to-time conversion constant	23
3.2.2 Pulse train generation	25
3.2.3 Temporal window and efficiency.....	27
3.3 Chirp in the DST Pulse Shaper	33
3.3.1 Chirp measurement	37

3.3.2	Diffraction analysis	39
3.3.3	Measurements.....	43
3.4	Multiple Output Channels	48
3.4.1	Mathematical description	48
3.4.2	Measurements.....	50
3.5	Summary of DST / FT Differences	52
4.	Integrated Optic Configuration	55
4.1	Background	56
4.2	DST / AWG Analogy.....	60
4.3	Pulse Train Generator.....	62
4.4	Integrated DST	67
5.	Future Directions.....	71
	List of References.....	75
	Appendix	81
	VITA	85

LIST OF TABLES

Table	Page
Table 3.1	52

LIST OF FIGURES

Figure	Page
Fig. 1.1. A target application of the DST pulse shaper.	3
Fig. 2.1. Fourier transform pulse shaping geometry.	5
Fig. 2.2. Schematic diagram of the 100Gbit/s testbed used in [48].	8
Fig. 3.1. The first 'DST' pulse shaping data (left) and spatial masking functions (right) reported by Froehly et. al. [22].	11
Fig. 3.2. Pulse shaping data reported by Sauteret et. al. [25].	12
Fig. 3.3. Schematic diagram of the DST pulse shaper.	14
Fig. 3.4. Trigonometric argument for determining the space-to-time conversion constant.	18
Fig. 3.5. Spectrometer analogy for the DST pulse shaper.	19
Fig. 3.6. Complete DST pulse shaping apparatus.	21
Fig. 3.7. Final DST apparatus with image plane viewing optics.	23
Fig. 3.8. Measurement of the space-to-time conversion constant.	24
Fig. 3.9. Measured pulse trains utilizing periodic pixelation masks.	26
Fig. 3.10. Two example 'pulse packets'.	27
Fig. 3.11. Calculated temporal window and optical efficiency as a function of pulse shaping slit width.	31

Figure	Page
Fig. 3.12. Shift in output center wavelength as a function of input pixelation slit position (in space and time). The slope provides a measure of the chirp on the output of the DST pulse shaper.	38
Fig. 3.13. Relevant planes considered in the diffraction analysis	40
Fig. 3.14. Measured chirp and space-to-time conversion constant as a function of pulse shaping lens-output slit separation.....	44
Fig. 3.15. Measured and calculated chirp for two interesting specific cases of the diffraction analysis result. Solid line is calculated and triangles are measured for grating-lens separation, $d_1 = f$, but lens-slit separation allowed to vary. Dashed line is calculated and squares are measured for lens-slit separation held fixed at the focal length of the pulse shaping lens while grating-lens separation is allowed to vary.....	45
Fig. 3.16. Calculated (lines) and measured (symbols) chirp in the general case.	46
Fig. 3.17. Intensity cross correlation measurements of the DST pulse shaper output for an 'optical packet' pixelation mask, and three values of output chirp. (A) is heavily chirped, (B) moderately, and (C) approximately chirp-free.....	47
Fig. 3.18. Output power spectra as a function of transverse pulse shaping slit position for a periodic pixelation mask.	50
Fig. 3.19. Intensity cross correlation measurements of the DST pulse shaper output for two different transverse positions of the pulse shaping slit separated by 2 mm.....	51

Figure	Page
Fig. 4.1. Photos of the bulk optics DST pulse shaper (left) and an AWG (right).	55
Fig. 4.2. AWG Structure.	56
Fig. 4.3. Filter design methodologies for (A) traditional AWG filters, and (B) DST pulse shaping using an AWG.....	59
Fig. 4.4. Experimental apparatus for AWG pulse train generation experiments.	63
Fig. 4.5. Measured power spectra from the 40 GHz output channel spacing AWG. Both the full wavelength span (left) and the expanded (right) curves are plotted on a semi-log scale to more readily show the multiple filter passbands.....	64
Fig. 4.6. Intensity cross correlation measurements of the 100 GHz output channel spacing (left) and 40 GHz output channel spacing (right) devices for output channels 3 (top) and 4 (bottom).	65
Fig. 4.7. Measured intensity cross correlation (solid) from the 100 GHz output channel spacing device overlaid with the calculated temporal window (dash).	66
Fig. 4.8. DST-AWG device schematic.....	68

ABSTRACT

Leaird, Daniel E. Ph.D., Purdue University, December, 2000. Direct Space-to-Time Pulse Shaping for Ultrafast Optical Waveform Generation. Major Professor: Andrew M. Weiner.

The high-speed photonic network industry, driven by the demands of enormous growth of network data traffic, has grown to be a multi-billion dollar entity. The availability of increased data traffic has come about due to the growth in bandwidth transmitted over optical fiber. This growth is primarily due to research in two areas – time-division-multiplexed (TDM), and wavelength-division-multiplexed (WDM) photonic network schemes. A key bottleneck in these high-speed photonic networks is the optical-electronic (OE) interface. Currently, multiple laser sources and/or multiple serial optoelectronic modulators are used to implement the OE interface in both photonic network schemes. In this thesis, an apparatus will be demonstrated that could act as a relatively simple OE interface for these high-speed photonic networks.

The optical system, a direct space-to-time (DST) pulse shaper, converts a 1-D spatially patterned short optical pulse directly into a serial ultrafast time-domain waveform in a configuration compatible with the use of high-speed reflection modulator arrays. The space-to-time conversion properties, chirp compensation/cancellation, and potential for multiple spatially separated but wavelength shifted outputs will be examined theoretically and experimentally.

Integrated optic implementations of the DST pulse shaper, based on a common high-speed WDM network component, will be investigated as well. Work on the bulk optics implementation of the DST shaper provides considerable insight into the operation of the integrated optics implementations. The space-to-time mapping, and multiple output channel characteristics of the bulk optics DST are shown to function similarly in the integrated optics implementations. These integrated optic versions of the DST pulse shaper may play a significant role in future high-speed photonic networks.

1. INTRODUCTION

The generation and control of pulses of light has been a fundamental quest of scientists and engineers in the field of optical science. Ever since the first laser was demonstrated, significant effort has been placed on the generation and control of laser pulses. Pulse durations have decreased steadily over the years; however, it was not until the realization of the colliding pulse modelocked (CPM) dye laser that laser pulses with durations measured in femtoseconds were available. With the availability of these ultrashort pulses and the incredible bandwidth they possess, scientists in the field of short pulse optics started in earnest to realize the optical analog of a fundamental electronic component – the function generator. Weiner and Heritage demonstrated the first truly general ultrashort pulse generator with the femtosecond Fourier transform (FT) pulse shaping apparatus [1]-[3]. They and other colleagues demonstrated the utility of the FT pulse shaping apparatus by employing it in diverse experiments in the fields of physics & chemistry [4]-[7], and optical communications [8]-[10]. The apparatus itself was enhanced as well - first with demonstrations of phase only coding for the generation of pulse trains with minimum loss [11], and later with the introduction of a liquid crystal modulator array that permitted electronically programmable optical pulse shapes with millisecond update rates [12]-[13]. Other pulse shaping schemes exist as well, employing acousto-optic modulators [14], electro-optic modulators [15], optical gating [16], or

engineered nonlinear devices [17]. However, the FT apparatus to date has permitted the most flexibility in pulse shape synthesis, and as such has been more widely employed than other techniques. Recent applications and advances of the FT pulse shaping apparatus include adaptive pulse compression in short pulse amplifiers [18],[19], dynamic holography in multiple quantum wells [20], and a ‘pulse shaper on a chip’ [21].

The breadth and depth of applications that have been enabled by the FT pulse shaping geometry in laboratories around the world are a testament to the usefulness and importance of this apparatus. For all the effort that has been put forth into understanding and using the FT pulse shaping apparatus, it seems interesting that virtually no effort has been spent investigating its cousin – the direct space-to-time (DST) pulse shaping apparatus. The DST apparatus [22]-[38], first introduced by Colombe et. al. in 1976 [22]-[27], differs from the FT pulse shaper in what at first may seem to be minor points (these issues will be explored in the next chapter). However, when one examines the geometry carefully, it becomes clear that this apparatus could have significant impact on how pulse shaping technology is employed in several fields – most notably optical communications. One possible system application for the DST pulse shaper is shown in Fig. 1.1. In this potential application, the DST pulse shaper, with an appropriately configured optoelectronic modulator array serves as the optical-electronic interface in a high-speed communication system. Parallel, electronic data streams can be serialized onto an ultrafast optical channel in this parallel-to-serial multiplexing application.

The remainder of this document will focus primarily on the DST pulse shaping geometry, and the issues related to its implementation. In order to provide a frame of reference for comparison, the FT pulse shaping geometry will be reviewed briefly at the

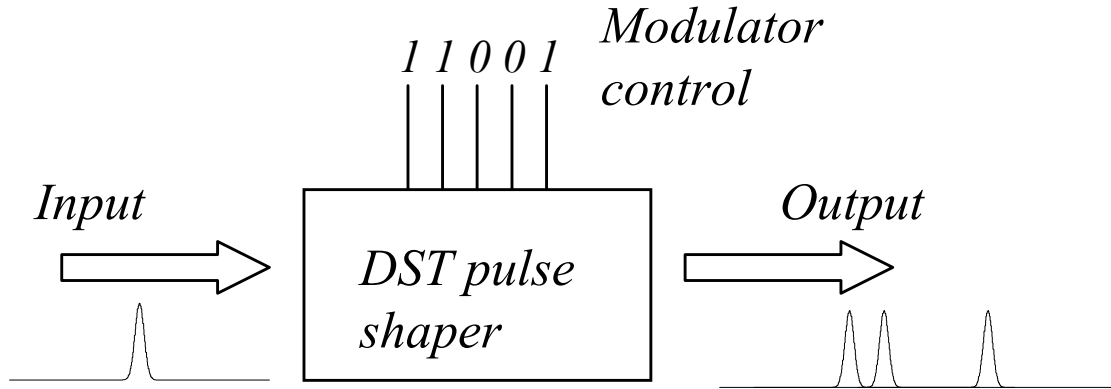


Fig. 1.1. A target application of the DST pulse shaper.

beginning of the next chapter. Following that, the DST pulse shaper will be presented in detail utilizing a bulk optics configuration. Specifically, femtosecond operation of a DST pulse shaper will be demonstrated in an arrangement that is compatible with the direct insertion of a high-speed optoelectronic modulator array. Analysis of the chirp compensation properties in the DST shaper including experimental confirmation of this analysis will also be demonstrated. Finally, the potential for multiple output waveforms with the same output intensity profile, but different center wavelengths will be demonstrated.

After discussing the bulk optics configuration of the DST pulse shaper, an integrated optic configuration of this apparatus, based on an arrayed-waveguide grating (AWG) [39],[40], will be discussed. This component, commonly used in dense wavelength division multiplexed optical networks, can be modified to perform the same space-to-time mapping as the DST pulse shaper implemented in bulk optics [41],[42]. After presenting the DST pulse shaper (implemented in bulk optics) in detail, the integrated implementation will be presented both for general 'optical packet' generation [41] as well as ultrafast pulse train generation [43]-[46] in a configuration slightly

modified as compared to [41]. Finally, the possibilities for future investigations with these devices will be discussed.

2. BACKGROUND

As mentioned in the introduction, the FT pulse shaping apparatus has enabled numerous applications in the field of ultrafast optics over the past 15 years. Since this apparatus is the ‘standard’ by which researchers in the field of ultrafast optics implement pulse shaping technology in their experiments, it would be remiss to fail to summarize this critical technology here. A schematic diagram of the FT pulse shaping geometry is shown in Fig. 2.1. The apparatus consists of two diffraction gratings, two lenses, and a spatially patterned mask that can contain amplitude and/or phase information. A short pulse incident on the input grating is dispersed – different frequency components within

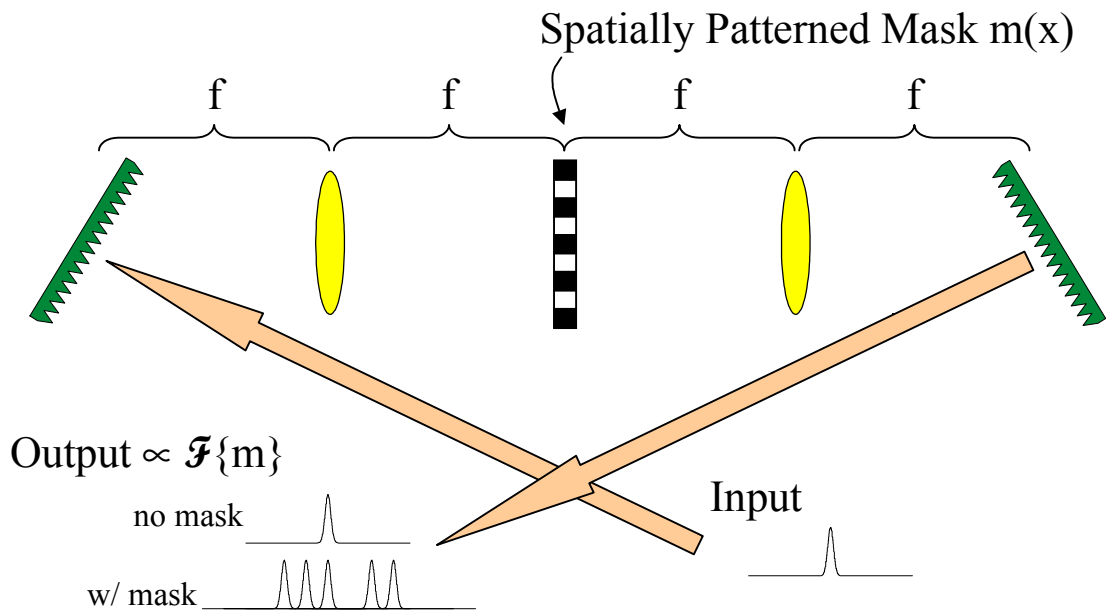


Fig. 2.1. Fourier transform pulse shaping geometry.

the pulse travel at different angles away from the diffraction grating. The first lens, which is placed a focal length away from the grating, stops the spatial dispersion, and focuses each 'individual' frequency component to a 'separate' spot at the focal plane of the lens – the so-called masking plane. The second lens and grating, placed as a mirror image of the first two components around the masking plane, serve to recombine all the frequency components into a single output beam. Provided that the apparatus is properly aligned, with no mask present at the masking plane, the output temporal shape is identical to the input shape – another way of saying that the apparatus is dispersion-free. Consider the fact that the frequency components which make up the short pulse that is incident onto the apparatus are spatially dispersed at the masking plane. With the frequencies separated in this manner, it is possible to manipulate individual frequency components using a spatially patterned mask. Spatially patterned masks manipulate the amplitude and/or phase of frequency components of the spectrum of the short pulse. Since the temporal profile of the short pulse is given by the Fourier transform of its spectrum, the temporal profile of the output pulse is given by a Fourier transform of the frequency spectrum transmitted through the spatially patterned mask(s) - hence the term Fourier Transform pulse shaper.

Fixed masks, patterned using photolithography operations similar to those used in the electronics industry for defining integrated circuits, were first used as pulse shaping masks. Amplitude masks are made by patterning an opaque film so that individual frequency components are either transmitted through a clear spot in the film, or blocked by an opaque region. Phase masks are made by defining a pattern on a transparent substrate (typically glass), and then reactive-ion etching the patterned substrate. In this

way ‘pits’ are formed on the substrate – the depth of the ‘pit’ relative to unetched regions of the active area, and the refractive index of the substrate determine the phase shift within that region. More simply put, the optical path length is spatially modulated within the phase mask – the optical path length difference determines the relative phase shift. Fixed masks have the advantage of providing a high degree of flexibility in the design of pulse shaping masks; however, the pulse-shape update rate is determined by how fast those fixed masks can be manipulated. In order to overcome this feature of fixed masks, Weiner and colleagues developed a new masking device based on liquid crystal technology [12],[13]. With this new ‘mask’, electronically programmable pulse processing was born. Now pulse shapes can be manipulated under computer control with the pulse-shape update rate determined by the relaxation time of the liquid crystal – on the order of 10’s of milliseconds. With the advent of the liquid crystal modulator, the field of femtosecond pulse processing saw radically increased interest. Currently, there are at least two commercial vendors of liquid crystal spatial light modulators for use in ultrafast pulse processing experiments, and the FT pulse shaping geometry is in use in numerous laboratories around the world.

While there are considerable application areas that have benefited from the use of the FT pulse shaper, there are some applications where the Fourier transform relation between the masking function and the temporal profile presents special difficulties that somehow must be overcome. For example, in time-domain multiplexed (TDM) communication systems, one could consider using a short pulse laser as input to a FT pulse shaper in order to generate pulse sequences to represent a packet of data. However, in order to generate the desired pulse sequence, the Fourier transform of the sequence

must be calculated, and modulated onto the spectrum using a high-speed optoelectronic modulator array. In general, to produce any arbitrary 'packet', both amplitude and phase modulation is required in the FT pulse shaper. Since current TDM systems, not based on FT pulse shaping operate at rates exceeding 100 Gb/s, calculating the Fourier transform of each 'packet' at these kinds of data rates presents special problems. Because of this difficulty, and a special interest in implementing high-speed optoelectronic pulse processing, a different pulse shaping geometry, coined the DST pulse shaper, has been explored. The characteristics of the DST pulse shaper will be presented in the next chapter.

It is worthwhile to note that significant work has been carried out in the past several years on related methods for generating high-speed optical data channels through wavelength division multiplexing (WDM), and time division multiplexing (TDM). Two recent examples illuminate the methods used in this research area. 1) A total capacity of 3 Tbit/s (19 wavelength channels separated by 480 GHz at 160 Gbits/s) has been transmitted over 40 km of dispersion shifted fiber [47]; although, only two 10 GHz

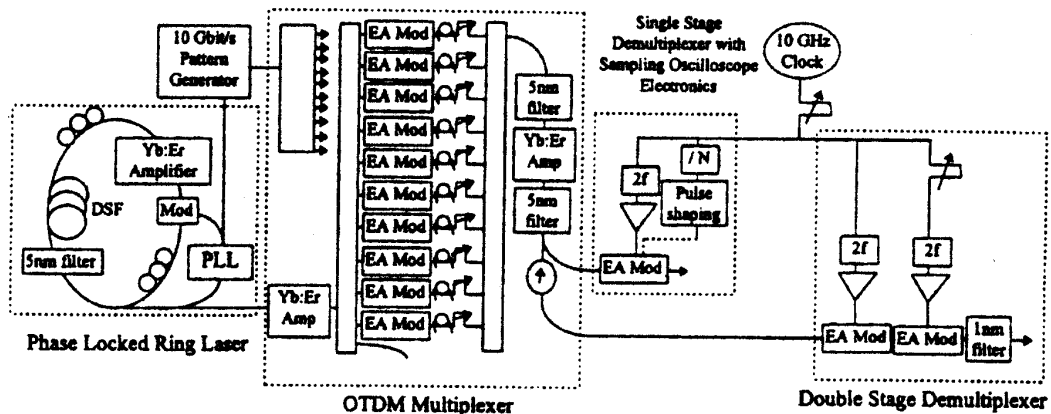


Fig. 2.2. Schematic diagram of the 100Gbit/s testbed used in [48].

source laser/modulator pairs were utilized to generate the full data stream. 2) Ten independent 10 GHz data streams (one laser and ten independent modulators) have been multiplexed to generate a single 100 GHz channel in order to explore channel cross-talk issues in high performance optical TDM networks [48]. The experimental configuration of this second case is shown in Fig. 2.2 as it is most closely related to a target application of the work presented here. Note that the parallel-electrical to serial-optical conversion operation demonstrated in [48] is carried out with individual fiber based variable optical delay lines which may prove cumbersome in a system implementation of this OE interface. As will be shown in the following chapters, the time-slot allocation in the final TDM output of the DST pulse shaper does not require individual channel control; rather, the space-time mapping of the pulse shaper directly controls the allocation without the need for dynamic adjustment.

3. DST BULK OPTICS CONFIGURATION

The DST pulse shaper was initially demonstrated in the mid-70's using ~ 30 psec pulses and fixed two-dimensional masks [22]. An example of the measured output pulse shapes and the spatial masks used in this early work is shown in Fig. 3.1. Interpreting this data as presented is difficult at best as the measurement technique used to record the temporal profiles appears not to have been documented. The only indication within the

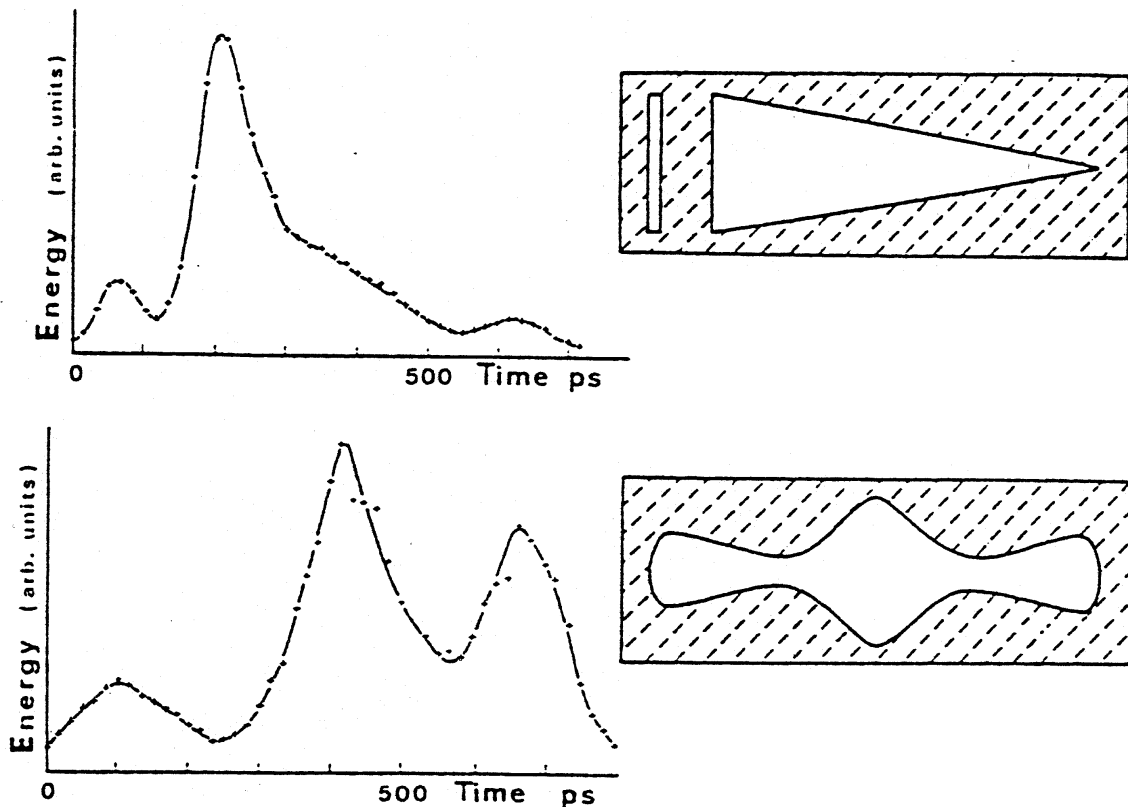


Fig. 3.1. The first 'DST' pulse shaping data (left) and spatial masking functions (right) reported by Froehly et. al. [22].

reference is a statement of "photometric recordings of energy repartition...". Clearly there is a difference in the recorded temporal profiles as a function of the spatial mask, and the output pulse durations appear to extend to ~ 700 ps; however, no other conclusions can be drawn from this information.

Roughly ten years later, the same group resurrected the pulse shaping geometry for use in dark soliton propagation studies in optical fibers [23] (incidentally, this

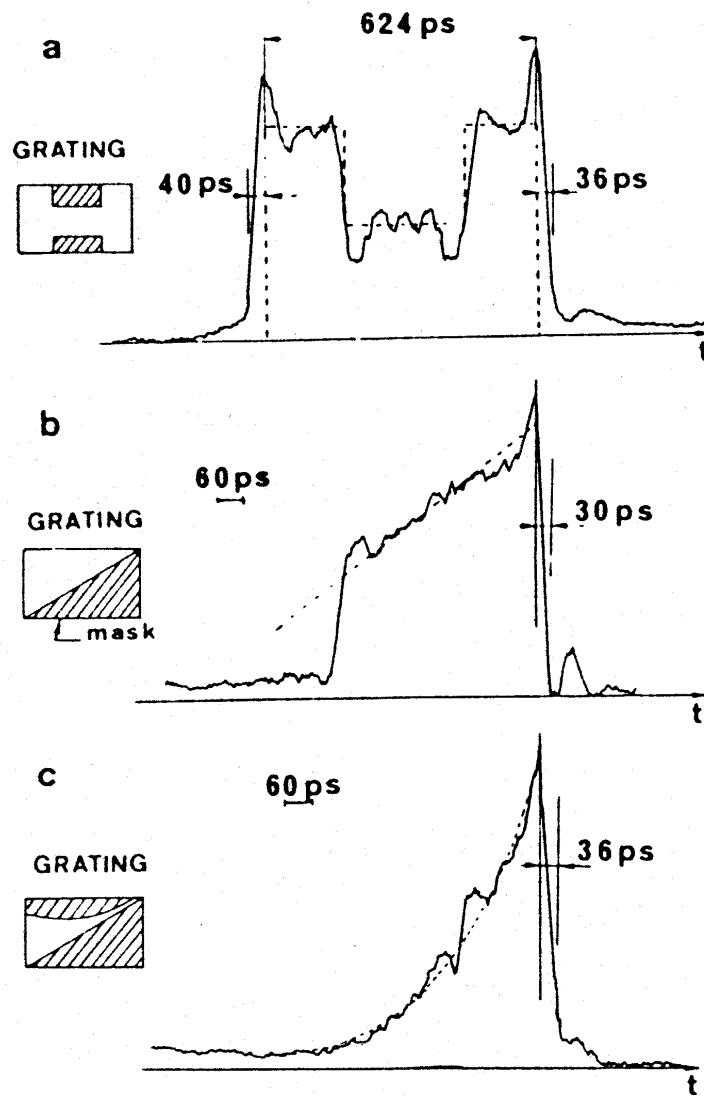


Fig. 3.2. Pulse shaping data reported by Sauteret et. al. [25].

occurred about the same time Weiner and colleagues were using the FT pulse shaper in similar studies [7]) – using pulses ~5 picoseconds in duration. This time more conventional measurement techniques were employed (intensity autocorrelation and power spectra), and more convincing data showing the effect of the space time mapping were included; although, the temporal window of the shaped output was limited to approximately a 30 ps window. Other reports using the DST shaper were also made around that same time period [24]-[27]. Perhaps the most convincing work was reported by another group of French researchers following on the work of Froehly et. al., utilizing amplified ~30 ps pulses to generate more complex output temporal profiles with features limited by the input pulse duration and utilizing approximately a 600 ps temporal window [25] (Fig. 3.2). No other reports are available regarding the use of such an apparatus until our recent application of the apparatus using femtosecond pulses while making it directly compatible with a high-speed optoelectronic modulator array [28],[29].

In an attempt to understand how the DST apparatus can be applied to ultrafast optical pulse sequence generation, we have illuminated issues critical to the design and implementation of a DST apparatus utilizing a one-dimensional (i.e. linear) masking function. These investigations have significantly expanded the understanding of this apparatus by exploring the issues of chirp compensation [30],[31],[33],[37],[38] and multiple spatially separated outputs with identical temporal intensity profiles but varying center wavelengths [33],[34],[36],[38]. A general description of the DST pulse shaper, and the space-time mapping of the apparatus will be presented first, both quantitatively and qualitatively. Then, the complete apparatus, as currently embodied, will be presented along with measurements of the space-time mapping, apparatus chirp, and multiple

spatially separated outputs. A mathematical framework will also be presented through which one may understand the design parameters of the apparatus.

3.1 DST Pulse Shaper Description

A schematic representation of the pulse shaping components making up the DST pulse shaper is shown in Fig. 3.3. A spatially patterned mask is present at the surface of a diffraction grating. A lens collects and focuses the spatially dispersed frequency components of the input beam that are diffracted from the grating. At the Fourier plane of the pulse shaping lens, a thin slit filters the dispersed spectrum, and in the ideal case generates a spatially homogeneous output beam whose temporal intensity profile is given by scaled replica of the spatial masking function present at the diffraction grating. The scaling parameter between the spatially patterned mask and the output temporal profile will be investigated in the next section.

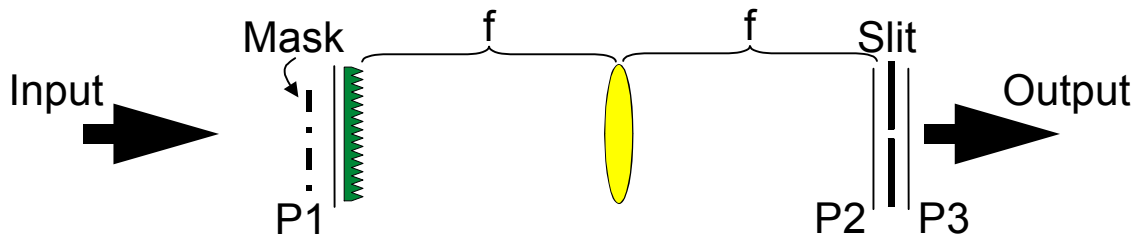


Fig. 3.3. Schematic diagram of the DST pulse shaper.

3.1.1 Quantitative argument

The Fourier transform relations used in all the following discussions are listed for completeness:

$$\begin{aligned}
 F(\omega) &= \frac{1}{\sqrt{2\pi}} \int dt f(t) \exp[-j\omega t] \\
 f(t) &= \frac{1}{\sqrt{2\pi}} \int d\omega F(\omega) \exp[j\omega t] \\
 S(k) &= \frac{1}{\sqrt{2\pi}} \int dx s(x) \exp[jkx] \\
 s(x) &= \frac{1}{\sqrt{2\pi}} \int dk S(k) \exp[-jkx]
 \end{aligned} \tag{3.1}$$

where ω and k are the optical and spatial frequencies respectively.

The key planes to be investigated in the following are shown in Fig. 3.3. If the input to the apparatus is an optical pulse of short duration with a spatial profile given by $s(x)$, then the field just before the diffraction grating is given by

$$e_1(x, t) = s(x) e_{in}(t) \propto s(x) \int d\omega E_{in}(\omega) \exp(j\omega t) \tag{3.2}$$

Here $e_{in}(t)$ is the temporal profile of the input field, its Fourier transform, $E_{in}(\omega)$ is the input spectrum, and x is the transverse spatial coordinate. Assuming a diffraction grating dispersion that is linear in space and frequency yields the spectrum just after the diffraction grating [49],[50]:

$$e_2(x, t) \propto s(x) \int d\omega E_2(x, \omega) \exp(j\omega t)$$

where

$$E_2(x, \omega) \propto s(\beta x) \exp(-j\gamma\omega x) E_{in}(\omega) \tag{3.3}$$

The spatial dispersion is written

$$\gamma = \frac{n \lambda}{c} \frac{d\theta_d}{d\lambda} = \frac{m \lambda}{c d \cos\theta_d} \tag{3.4}$$

where λ is the center wavelength, c is the speed of light, d is the period of the diffraction grating, θ_d is the angle of diffraction, m is the diffraction order ($m = 1$ here)

and n is the index of refraction ($n = 1$ is assumed throughout the remainder of this chapter). The astigmatism of the diffracting grating is included with the term

$$\beta = \frac{\cos \theta_i}{\cos \theta_d} \quad (3.5)$$

with the incident angle given by θ_i . If the grating-lens, and lens-output slit separations are set equal to the focal length of the lens, f , then the field just before the output slit is the spatial Fourier transform of eqn. (3.3) [51].

$$e_3(x, t) \propto \int d\omega E_{in}(\omega) S\left(\frac{2\pi x}{\beta \lambda f} - \frac{\gamma \omega}{\beta}\right) \exp(j\omega t) \quad (3.6)$$

Assuming an ideal thin slit at the apparatus output, and calling the transverse output slit position $x = 0$ for mathematical convenience yields the spectrum just after the output slit:

$$e_4(x, t) \propto \int d\omega E_{in}(\omega) S\left(-\frac{\gamma \omega}{\beta}\right) \exp(j\omega t) \quad (3.7)$$

Finally, the output temporal profile is determined by the Fourier transform of the output spectrum:

$$e_4(t) \propto e_{in}(t) * s\left(\frac{-\beta}{\gamma} t\right) \quad (3.8)$$

In words then, the output temporal profile is determined by the input field convolved with a scaled representation of the input spatial profile. The space-to-time conversion constant is given by

$$\frac{\gamma}{\beta} = \frac{\lambda}{c d \cos \theta_i} \quad (3.9)$$

The spatial profile just before the surface of the diffraction grating is the product of the masking function with the input beam profile. For a Gaussian beam we can write

$$s(x) = m(x) \exp\left[\frac{-x^2}{w^2}\right] \exp\left[\frac{-j k}{2 R} x^2\right] \quad (3.10)$$

where w is the Gaussian beam radius, and R is the phase front radius of curvature.

The first term, $m(x)$, represents the masking function just prior to the surface of the diffraction grating. The second term is the Gaussian spatial profile of the input beam, and the final term is a quadratic phase dependence which arises when the beam is not perfectly collimated at the grating. When eqn. (3.10) applies, the output temporal profile is rewritten

$$e_{\text{out}}(t) \approx e_{\text{in}}(t) * \left\{ m\left(\frac{-\beta t}{\gamma}\right) \exp\left[\frac{-\beta^2 t^2}{\gamma^2 w^2}\right] \exp\left[\frac{-j k \beta^2 t^2}{2 R \gamma^2}\right] \right\} \quad (3.11)$$

The term inside the $\{\dots\}$ is the impulse response function of the DST shaper. It consists of a scaled version of the mask, multiplied by a Gaussian temporal window function corresponding to the input Gaussian beam profile as well a quadratic temporal phase variation which arises when the phase front at the grating is not planar. In the remainder of this section we concentrate on the intensity behavior of shaped output. In section 3.3 we discuss the chirp corresponding to the quadratic temporal variation as well as its compensation.

3.1.2 Qualitative argument

Alternative descriptions of the basic operation of the DST shaper can be obtained by exploring the fundamental pulse shaping components and configuration shown in Fig. 3.3. First, the space-to-time conversion constant, γ/β , can equally be determined by examining the pulse-tilt for a collimated plane wave diffracted off a grating [52]. The

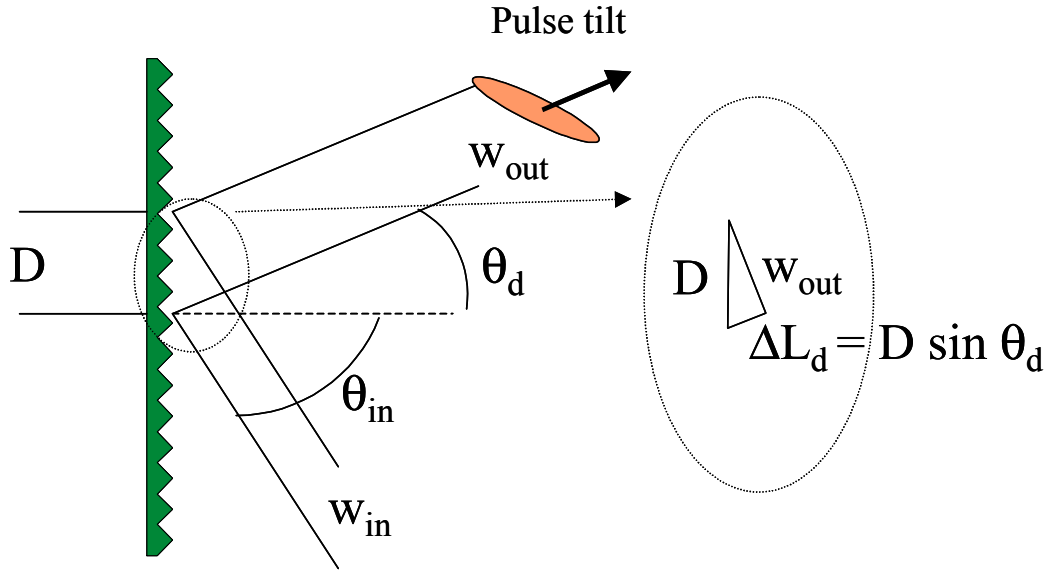


Fig. 3.4. Trigonometric argument for determining the space-to-time conversion constant.

pulse-tilt due to the angular dispersion of the grating (shown in Fig. 3.4), or delay across the diffracted beam relative to the input beam size derived from [52] or a simple trigonometric argument exactly gives the space-to-time conversion constant, eqn. (3.9).

The trigonometric argument for determining the pulse tilt is shown in Fig. 3.4. The magnitude of the path length difference, ΔL , in diffracting off the grating is given by

$$|\Delta L| = \Delta L_d - \Delta L_i = D \sin \theta_d - D \sin \theta_i \quad (3.12)$$

where the 'i' and 'd' subscripts represent the incident and diffracted beams. Using the grating equation,

$$\sin \theta_d = \sin \theta_i + \frac{m \lambda}{d} \quad (3.13)$$

the magnitude of the time delay experienced in diffracting off the grating is given by

$$|\Delta \tau| = \frac{|\Delta L|}{c} = \frac{\lambda D}{c d} \quad (3.14)$$

The astigmatism of the grating, as given by eqn. (3.5), is apparent from this argument as well:

$$\beta = \frac{w_{in}}{w_{out}} \quad (3.15)$$

The magnitude of the time delay across the beam relative to the input beam size exactly gives the space-to-time conversion constant shown in eqn. (3.9).

$$\frac{|\Delta\tau|}{w_{in}} = \frac{\lambda}{c d \cos \theta_i} \quad (3.16)$$

Second, the configuration shown in Fig. 3.3 will be recognized as a spectrometer arrangement with the addition of a spatially patterned mask on top of the diffraction grating. If a spectrometer (without a spatially patterned mask) is configured for maximum spectral resolution (large beam on the diffraction grating, and thin output slit), the output obviously consists of a narrow spectral feature. If the input consists of a short temporal duration optical pulse; then, the output pulse, in time, is broadened with respect to the input due to the spectral filtering performed by the spectrometer, as shown at the

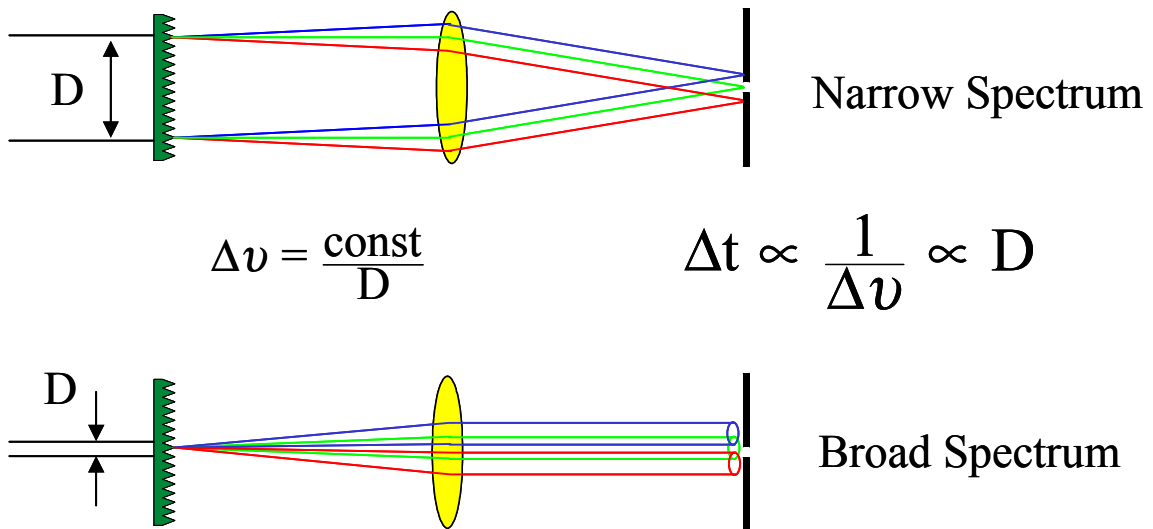


Fig. 3.5. Spectrometer analogy for the DST pulse shaper.

top of Fig. 3.5. Now if the apparatus configuration is unperturbed except that the size of the input beam is decreased, as shown at the bottom of Fig. 3.5, the resolution of the spectrometer is decreased as well. If one considers the input to be a short optical pulse again; then, the output spectrum is broadened with respect to the previous case, or the temporal duration of the output is decreased with respect to the previous case. The width of a mask which simply modifies the spatial extent of the beam on the diffraction grating can then be seen to modify the temporal duration of the apparatus output directly. This argument illustrates the operation of the DST pulse shaper in a very simple case and shows its relation to a classical optical spectrometer. In the following sections, we will extend these results to understand the femtosecond response of a generalized spectrometer, allowing generation of complex optical waveforms, control and compensation of chirp, and the possibility of obtaining multiple wavelength-shifted versions of a femtosecond pulse sequence simultaneously.

3.2 Complete Apparatus

The schematic representation of the DST pulse shaper shown in Fig. 3.3 is convenient for understanding the space-time mapping of the apparatus; however, in practice a slightly more complex apparatus provides substantial additional flexibility. The complete DST pulse shaping apparatus is shown in Fig. 3.6. The pulse shaping components discussed in the previous section are present to the right of the dashed line while the mask generation optics are to the left of the dashed line. For the experiments to be discussed in the following, a Ti:S laser producing 100 fs pulses at a center wavelength of 850 nm is used as the input to the DST pulse shaper.

The output beam from the source laser is spatially patterned by transmission through a fixed amplitude mask consisting of a one-dimensional array of transparent rectangles in an otherwise opaque background. The spatially patterned beam at the ‘pixelation plane’ is imaged by the lens L1, a 100 mm focal length condenser lens, onto the ‘modulation plane’ through a polarizing beamsplitter cube and quarter-wave plate. The size (20 μm square) and pitch (62.5 μm center-to-center) of the transparent elements in the fixed mask as well as the imaging condition of the first lens have been selected to provide direct compatibility with a high-speed optoelectronic reflection modulator array. This feature is included so that, in future experiments, individual spatial locations may be set to either a high reflectivity state or a low state in a programmable fashion. For the work described here, the ‘modulation plane’ consists of a simple mirror. The spatially patterned beam reflected from the ‘modulation plane’ is imaged, back through the quarter-wave plate/polarizer combination onto the diffraction grating (1800 lines/mm) by

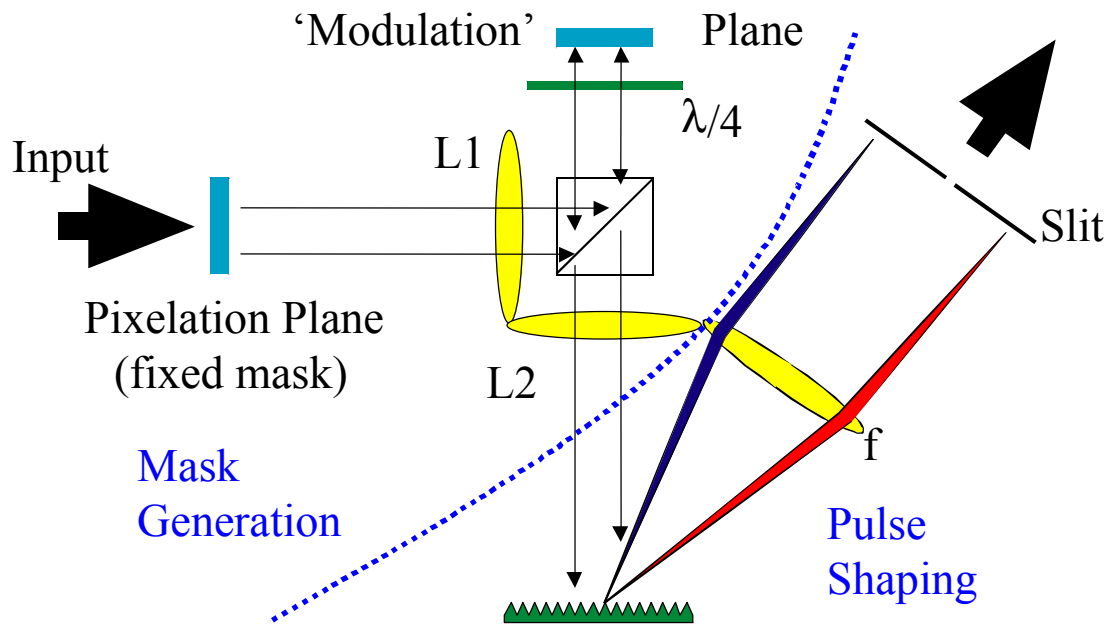


Fig. 3.6. Complete DST pulse shaping apparatus.

the lens L2, a 75 mm focal length condenser lens. The pulse shaping lens is a 160 mm focal length acromat. The function of all the mask generation optics is to transfer a one-dimensional spatially patterned intensity profile from the apparatus input to the diffraction grating. The space-to-time conversion constant, γ/β , is referenced to the surface at, but before diffracting off, the grating. In order to relate γ/β to the apparatus input, Eqn. (3.9) must be multiplied by *mag*, the overall imaging system magnification of the mask generation optics.

In order to ensure high quality output pulse shapes, it is important to verify the quality of the images present at both the 'modulation plane' and the diffraction grating. This is accomplished by viewing the image planes with a CCD camera and telephoto lens. At the grating, the image is large enough, and surrounding optical table space ample enough that a mirror can be inserted next to the grating to relay the image of the grating surface vertically (out of the plane of the table) so that it may be viewed with the camera. At the modulation plane, verifying the image quality is a much more difficult task. Due to the number of components in the area, inserting an out-of-plane viewing mirror, as was done for viewing the grating surface, is not practical. A thin plate beamsplitter was inserted between the 'modulation plane' and the quarter-wave plate in order to facilitate out-of-plane viewing; however, alignment was difficult given the small features present in the 'modulation plane' image (20 μm pixels on 62.5 μm pitch) . Further, when acceptable alignment was obtained, the image plane was difficult to observe due to saturation of the CCD camera. The final solution for observing the 'modulation plane' was to insert another polarizing beamsplitter cube between the first imaging lens (L1) and the beamsplitter shown in Fig. 3.6. In this manner, the image of

the 'modulation plane' could be viewed on-axis (minimizing viewing aberrations) without saturating the CCD camera. This configuration is shown in Fig. 3.7.

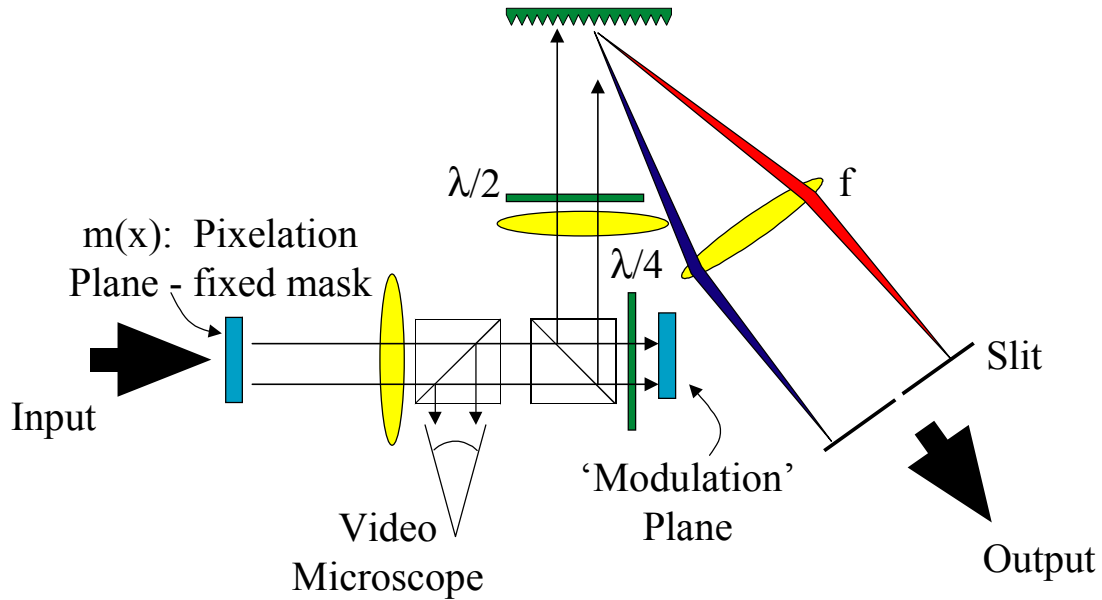


Fig. 3.7. Final DST apparatus with image plane viewing optics.

Measurements of the output temporal intensity profile from the DST pulse shaper were carried out via intensity cross correlation with a reference pulse directly from the source laser. In order to ensure reasonable second-harmonic conversion in the nonlinear crystal used in the cross-correlator, it was necessary to include a cylindrical lens after the output slit. The image of the focused signal (DST output) and reference beams was monitored at the nonlinear crystal, and optimum spatial overlap was obtained by adjusting the distance between the cylindrical lens and the pulse shaper output slit.

3.2.1 Measuring the space-to-time conversion constant

A simple measurement of the space-to-time conversion constant, and a first example of pulse shaping with the DST is shown in Fig. 3.8. A thin slit replaces the

spatially patterned mask at the ‘pixelation plane’, and intensity cross-correlations are recorded of the output pulses, using a reference pulse directly from the source laser, for several different transverse positions of the slit at the pixelation plane. The delay shift between traces gives a measurement of the space-to-time conversion constant including the imaging system magnification. In the top series of Fig. 3.8, a 25 μm slit is moved $\pm 80 \mu\text{m}$ from the center of the input beam with an imaging system magnification of 4.2. Measuring the change in delay from one trace to the next gives a measured space-to-time conversion constant of 29.6 ps/mm. Using the measured diffraction angle of the grating (54°), the expected space-to-time conversion constant is calculated to be 30.7 ps/mm. A second example of measuring the space-to-time conversion constant is given in the bottom curves of Fig. 3.8. In this case, a 20 μm slit is translated in 250 μm increments across the pixelation plane with an imaging system magnification of 6.5. The measured space-to-time conversion constant is 47.0 ps/mm in excellent agreement with the calculated value of 47.5 ps/mm.

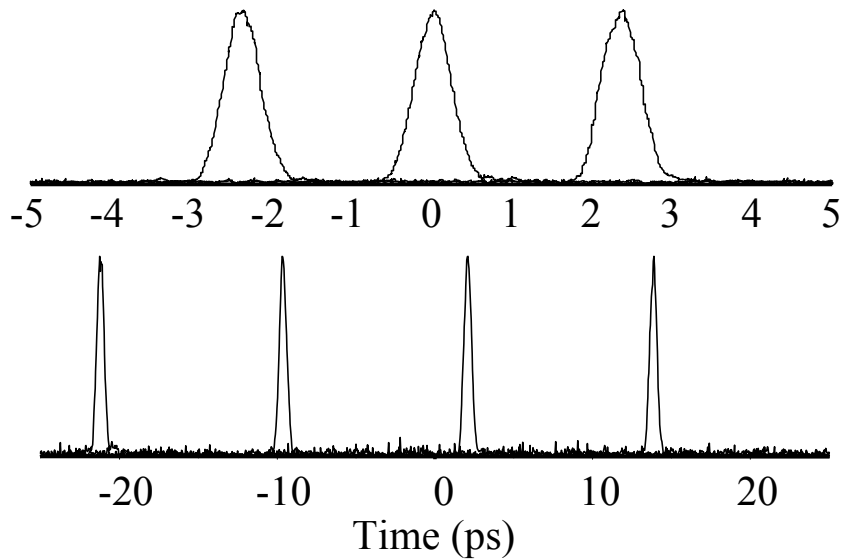


Fig. 3.8. Measurement of the space-to-time conversion constant.

3.2.2 Pulse train generation

One target application of the DST pulse shaper is in the generation of trains of pulses, or pulse sequences, where the state of each pulse in the train, either ‘ON’ or ‘OFF’, is set by the optical transmission at a specific spatial location. In order to demonstrate the pulse train generation capabilities of the DST pulse shaper, a periodic fixed mask is inserted at the pixelation plane. Fig. 3.9 shows the output pulse shapes, recorded by intensity cross-correlation for two different periodic pixelation patterns and an imaging system magnification of 4.2. Fig. 3.9A corresponds to a mask with 20 transparent rectangles 20 μm wide with 62.5 μm center-to-center spacing. This mask generates a train of 20 pulses. The pulse period, 1.88 ps, is in excellent agreement with the value expected from the space-to-time conversion constant, 7.3 ps/mm, and imaging system magnification. Fig. 3.9B shows a similar case where every other transparent feature of the pixelation mask is blocked. As expected, a train of ten pulses with twice the period of the previous case is measured at the apparatus output. In both of these cases, the output pulse train is observed to be superimposed on a roughly Gaussian window. The roll-off in the temporal profile is due to the input beam profile at the pixelation mask, and the extent of the temporal window is determined from the input beam profile and the effect of the finite width pulse shaping slit as will be discussed in the following section. If a uniform pulse train is desired, a diffractive optical element (DOE) could be used instead of the pixelation mask as a ‘spot-generator’ [53].

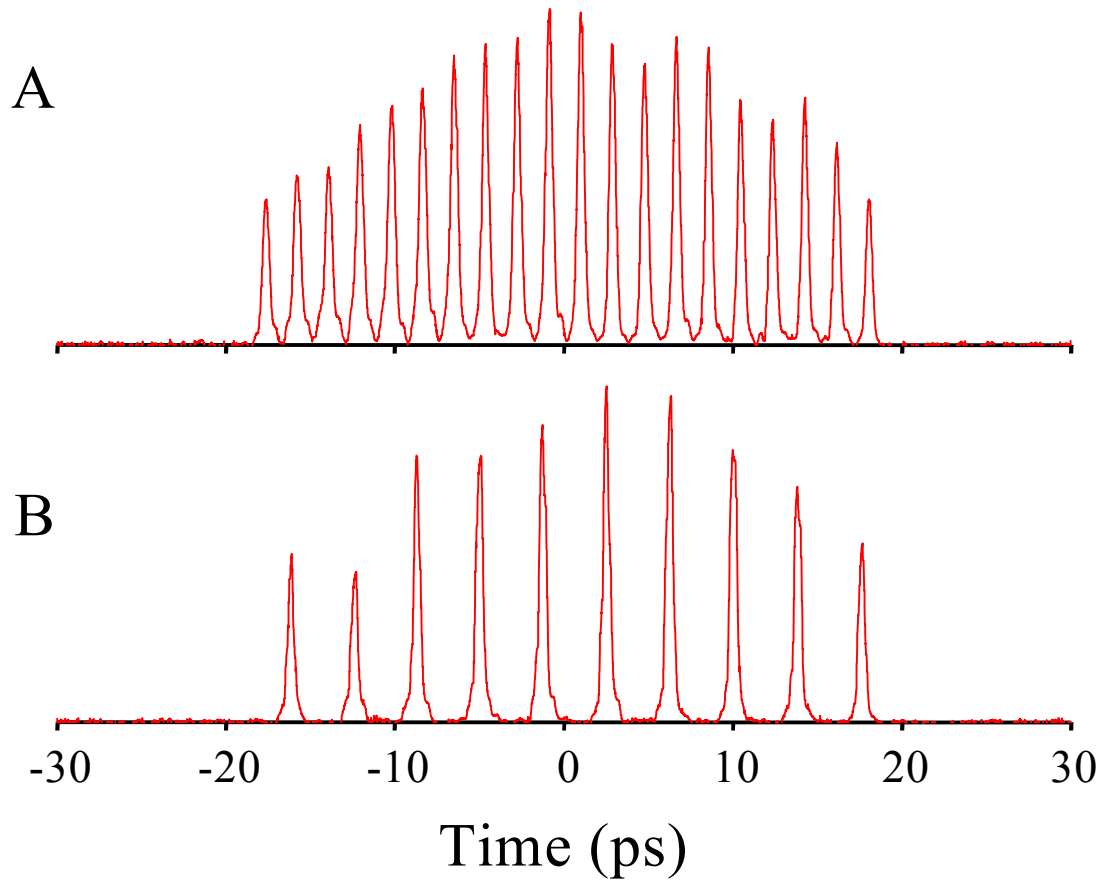


Fig. 3.9. Measured pulse trains utilizing periodic pixelation masks.

Fig. 3.10 shows two final examples of pulse sequence generation with the DST apparatus. In these cases, individual spatial locations within the 20 element pixelation mask are blocked. The resulting DST output, again recorded via intensity cross correlation with a short reference pulse directly from the source laser, is a ‘pulse packet’. This data demonstrates the parallel-to-serial conversion property of the DST pulse shaper that may play an important role in optical communications. All of the data shown here have been generated using a fixed pixelation mask to control the spatial pattern present at the diffraction grating. Equivalently, an optoelectronic modulator array could be used at the ‘modulation plane’ shown in Fig. 3.6 in order to electronically control the

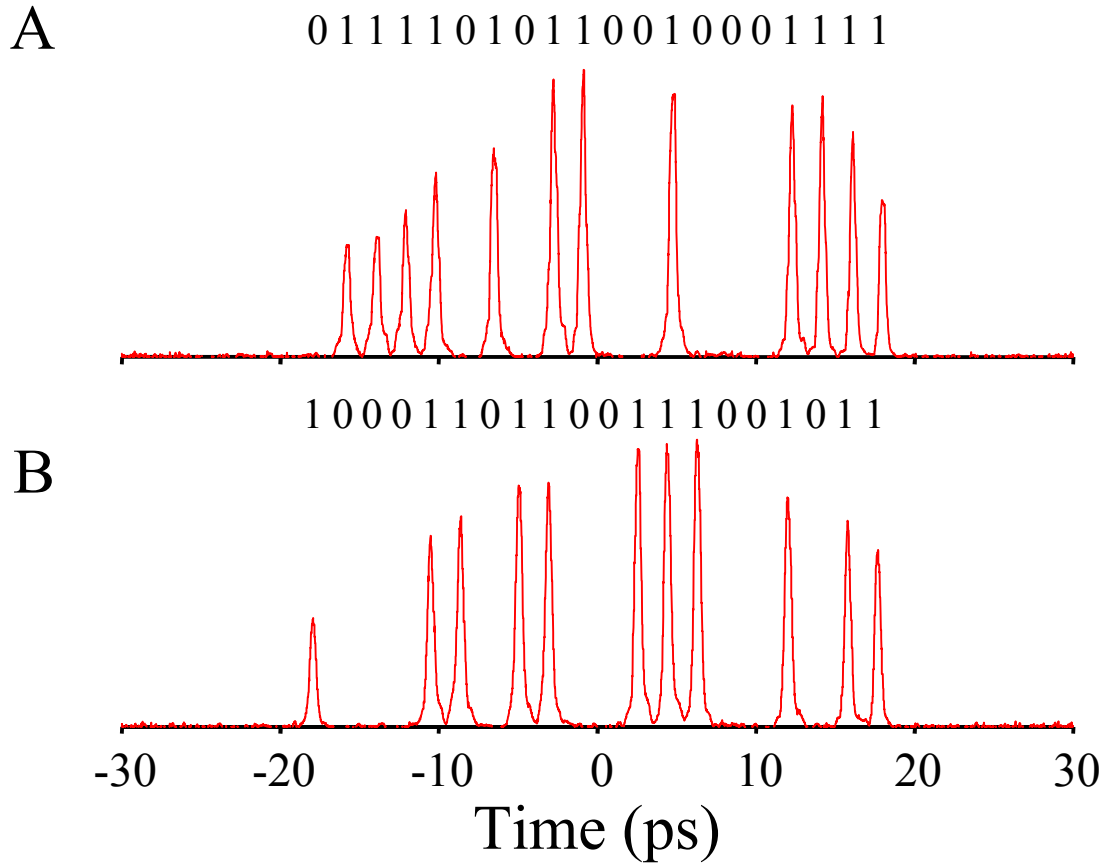


Fig. 3.10. Two example 'pulse packets'.

transmission of each spatial location. Of course, the excellent ON-OFF contrast apparent in Fig. 3.9 and Fig. 3.10 would then be limited by the actual contrast provided by the modulator array.

3.2.3 Temporal window and efficiency

In the mathematical descriptions presented thus far, a very thin (delta function) slit has been utilized at the output of the DST apparatus. Although this provides an ideal pulse shaping response, it is not practical, since the transmitted power would be zero. In the following, a finite width output slit is introduced which will be shown to impact the optical efficiency and pulse shaping temporal window.

First, recall that the field just prior to the output slit is determined by the input spectrum multiplied by the Fourier transform of the masking function, eqn. (3.6) when the grating-lens and lens-slit separations are equal to the focal length of the pulse shaping lens (this restriction will be relaxed in section 3.3 leading to interesting consequences for the chirp of the DST output). Eqn. (3.6) is repeated here for the readers' convenience.

$$e_3(x, t) \propto \int d\omega E_{in}(\omega) S\left(\frac{2\pi x}{\beta\lambda f} - \frac{\gamma\omega}{\beta}\right) \exp(j\omega t) \quad (3.6)$$

Now a general slit with amplitude transmittance $a\left(\frac{x}{x_o}\right)$, where x_o allows the width of the slit to be scaled, is inserted. The field after the slit is now given by:

$$e_4(x, t) \propto \int d\omega a\left(\frac{x}{x_o}\right) E_{in}(\omega) S\left(\frac{2\pi x}{\beta\lambda f} - \frac{\gamma\omega}{\beta}\right) \exp(j\omega t) \quad (3.17)$$

Unlike the case of a delta-function slit, the field is now a nonseparable function of space and time; the actual field seen by an experiment depends on where the experiment is placed and any spatial filtering between the DST output slit and the experiment. In many cases it will be the on-axis field after diffraction into the far field that will be of interest. This situation is easily treated analytically, since the diffraction into the far-field is equivalent to a spatial Fourier transform, which should be evaluated at $x=0$ to obtain the on-axis field. The one-dimensional far-field (Fraunhofer) diffraction integral is [56]:

$$\psi(x) = \frac{j}{\lambda L} \exp(-j k L) \exp\left(\frac{-j k x^2}{2L}\right) \int_{-\infty}^{\infty} dx' \psi(x') \exp\left(\frac{j k}{L} x x'\right) \quad (3.18)$$

where the primed variable is the source coordinate, the unprimed variable is the observation coordinate, and L is the distance between them. Using this relation, the output spectrum is given by:

$$E_{\text{out}}(\omega) \propto E_{\text{in}}(\omega) \left[S\left(\frac{-\gamma \omega}{\beta}\right) * a\left(\frac{\lambda \gamma f \omega}{2\pi x_0}\right) \right] \quad (3.19)$$

Once again, $S(k)$ is the Fourier transform of the spatial profile at the diffraction grating. The output temporal profile is then given by the Fourier transform of Eqn. (3.19)

$$e_{\text{out}}(t) \propto e_{\text{in}}(t) * \left[s\left(\frac{-\beta t}{\gamma}\right) A\left(\frac{2\pi x_0 t}{\lambda \gamma f}\right) \right] \quad (3.20)$$

where $A(k)$ is the Fourier transform of the slit function.

In the case of a perfectly collimated input beam ($R = \infty$), the output field can be rewritten in terms of the masking function, $m(x)$, and the input Gaussian beam profile, which gives the following:

$$E_{\text{out}}(\omega) \propto E_{\text{in}}(\omega) \left[M\left(\frac{-\gamma \omega}{\beta}\right) * \left\{ \exp\left(\frac{-\gamma^2 w^2 \omega^2}{4\beta^2}\right) * a\left(\frac{\lambda \gamma f \omega}{2\pi x_0}\right) \right\} \right] \quad (3.21)$$

and

$$e_{\text{out}}(t) \propto e_{\text{in}}(t) * \left[m\left(\frac{-\beta t}{\gamma}\right) \exp\left(\frac{-\beta^2 t^2}{\gamma^2 w^2}\right) A\left(\frac{2\pi x_0 t}{\lambda \gamma f}\right) \right] \quad (3.22)$$

corresponding to output spectrum (3.19) and output temporal profile (3.20) just after the generalized output slit.

It is convenient to examine Eqn. (3.20) to analyze the effect a finite slit has on the output temporal profile. Provided that the input pulse duration is short compared to the output temporal duration, the temporal extent of the output is dominated either by the

scaled representation of the spatial profile at the diffraction grating, $s\left(\frac{-\beta}{\gamma}t\right)$, or the width of the slit through the term $A\left(\frac{2\pi x_o t}{\lambda \gamma f}\right)$. Of course, the optical power through the slit is expected to increase as the pulse shaping slit is opened although the exact form of the optical efficiency may not be obvious from eqns. (3.21) or (3.22).

A simple measure of efficiency can be calculated by integrating the power coming through the slit relative to the total power before the slit.

$$\eta = \frac{\iint dx d\omega \left| S\left(\frac{2\pi x}{\beta\lambda f} - \frac{\gamma\omega}{\beta}\right) E_{in}(\omega) a\left(\frac{x}{x_o}\right) \right|^2}{\iint dx d\omega \left| S\left(\frac{2\pi x}{\beta\lambda f} - \frac{\gamma\omega}{\beta}\right) E_{in}(\omega) \right|^2} \quad (3.23)$$

This expression does not take into account any spatial selection of the diffracted output field by the experiment but is useful as an upper limit to the available output power.

Fig. 3.11 shows the calculated temporal window (in terms of the FWHM of the intensity) and efficiency as a function of pulse shaping slit width. The space-to-time conversion constant was set to 7.3 ps/mm with unity imaging system magnification, and the input beam shape was a simple Gaussian beam with radius $w = 1.0$ mm just before the grating when calculating the temporal window. For slit widths below approximately 20 microns, the temporal window is limited only by the Gaussian beam size and is nearly independent of slit width. Thus, in this calculation the approximation of a delta-function output slit is valid for slit widths up to ~ 20 μm . Significantly above this value the temporal window decreases roughly inversely with the slit width.

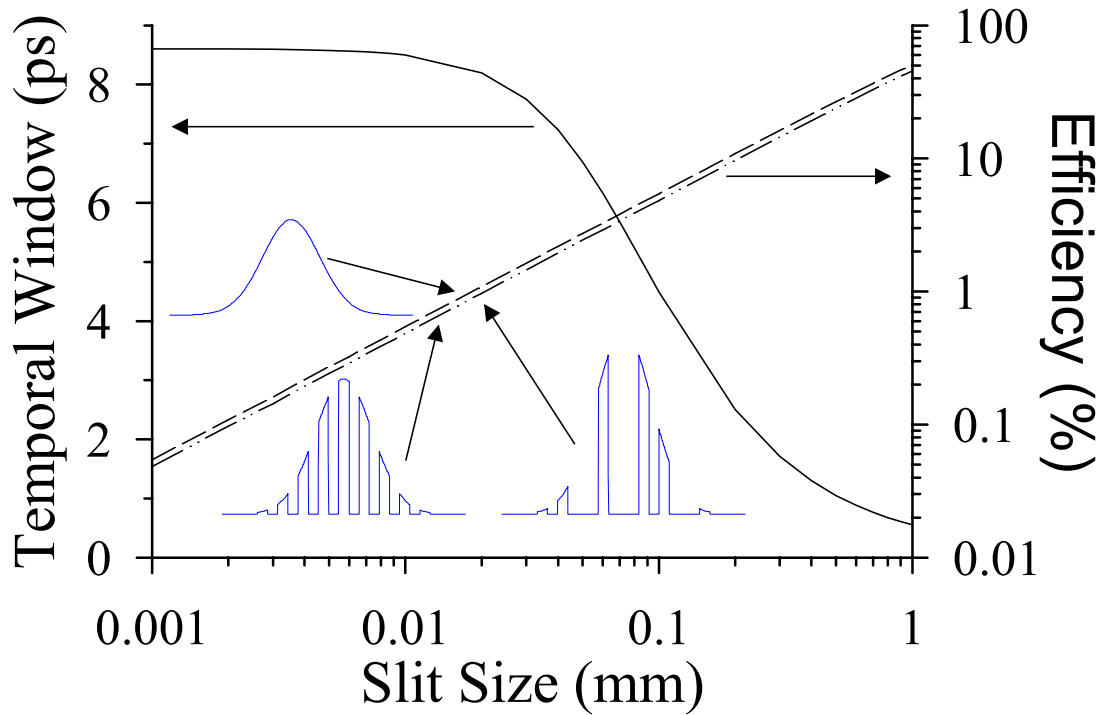


Fig. 3.11. Calculated temporal window and optical efficiency as a function of pulse shaping slit width.

The calculated result for the efficiency is also shown in Fig. 3.11 assuming a 300 fs duration (FWHM) transform limited Gaussian input pulse and three different input spatial profiles. First consider the case of no pixelation mask, i.e., a simple Gaussian spatial input profile (dashed line) as discussed with regards to the temporal window. The efficiency increases linearly as the slit width increases. Note that when a transform limited input pulse of duration t_p is spectrally sliced to generate a longer bandwidth limited pulse of duration T , the best case efficiency scales as t_p / T times a numerical factor of order unity. The DST pulse shaper achieves this best case for wide slit widths when the temporal window is determined mainly by the slit width. In this limit T is proportional to the inverse of the slit width, and therefore the efficiency is proportional to

the inverse of T . When the slit width is decreased below the regime where the spectral resolution and temporal window are limited by the slit, further reduction of the slit width reduces the efficiency without improving the temporal window. In this case the best case efficiency is not achieved. Therefore, for optimum efficiency the slit width should be adjusted to the largest width consistent with the required temporal window.

Fig. 3.11 also shows the result of efficiency calculations for two other spatial input patterns. One case is a periodic spatial masking function consisting of $250\ \mu\text{m}$ wide clear apertures with a $500\ \mu\text{m}$ period. The other case is an example of a pulse packet where some of the clear apertures in the periodic masking function are made opaque. The inset of Fig. 3.11 shows the input spatial field profile used in the calculation in each of the three cases including the unmasked Gaussian beam. The efficiencies are essentially indistinguishable for the two masked cases (dash-dot lines), which are also very close but slightly below the efficiency in the unmasked case. The integrated intensity in the input masked spatial profile is held constant in each case as would be the case if a DOE is used to spatially pattern the input beam without loss. If loss is incurred in shaping the input spatial profile, e.g. by using an amplitude mask, this reduces the overall system efficiency to a level below that predicted by eqn. (3.23). Notice that, for a fixed input pulse and temporal window, the efficiency is roughly independent of the masking function.

3.3 Chirp in the DST Pulse Shaper

The imaging operations shown in Fig. 3.6 have one side effect that has thus far not been discussed: in addition to relaying the desired intensity profile of the pixelated input beam onto the diffraction grating, the imaging operation places a quadratic spatial phase variation on the grating as well. The space-to-time conversion property of the DST pulse shaper operates on this spatial phase variation as well as on the intensity profile. The quadratic spatial phase is transformed into a quadratic temporal phase on the output waveform, and hence a chirp.

The magnitude and sign of the chirp attributable to the apparatus itself can be calculated if we assume a very short input pulse and assume $m(x) = 1$, i.e., there is no pixelation mask. Then eqn. (3.11) can be simplified to the following assuming a thin slit.

$$e_{\text{out}}(t) \approx \exp\left(\frac{-\beta^2 t^2}{\gamma^2 w^2}\right) \exp\left(\frac{-j k \beta^2 t^2}{2 R \gamma^2}\right) \quad (3.24)$$

This is of the form

$$e(t) \propto \exp(-\Gamma t^2) \quad (3.25)$$

where Γ has both real and imaginary parts.

$$\Gamma = \Gamma_r + j \Gamma_i \quad (3.26)$$

with

$$\Gamma_r = \frac{\beta^2}{\gamma^2 w^2} \quad (3.27)$$

and

$$\Gamma_i = \frac{k \beta^2}{2 R \gamma^2} \quad (3.28)$$

Then, consider the Fourier transform pair relating the temporal representation of the field to the spectral domain:

$$e(t) \propto \exp(-\Gamma t^2) \Leftrightarrow E(\omega) \propto \exp\left(\frac{-\omega^2}{4\Gamma}\right) \quad (3.29)$$

The frequency dependent phase is then given by

$$\phi(\omega) = \frac{\Gamma_i \omega^2}{4(\Gamma_r^2 + \Gamma_i^2)} \quad (3.30)$$

The frequency dependent delay is given by

$$\tau(\omega) = \frac{-\partial\phi}{\partial\omega} = \frac{-\Gamma_i \omega}{2(\Gamma_r^2 + \Gamma_i^2)} \quad (3.31)$$

and the chirp is given by the derivative of $\tau(\omega)$ with respect to frequency:

$$\frac{\partial\tau}{\partial\omega} = \frac{-\Gamma_i}{2(\Gamma_r^2 + \Gamma_i^2)} \quad (3.32)$$

Finally, it is convenient to express the chirp in terms of wavelength instead of frequency with the result

$$\frac{\partial\tau}{\partial\lambda} = \frac{\pi \Gamma_i c}{\lambda^2 (\Gamma_r^2 + \Gamma_i^2)} \quad (3.33)$$

Expressed in terms of the fundamental parameters, the chirp is given by

$$\frac{\partial\tau}{\partial\lambda} = \frac{\pi^2 c \gamma^2 R w^4}{\lambda \beta^2 (\lambda^2 R^2 + \pi^2 w^4)} \quad (3.34)$$

With this result it is possible to calculate the chirp expected to be present on the output of the DST pulse shaper in terms of the phase front radius of curvature, R , and beam size, w , at the diffraction grating as well as the space-to-time conversion constant, γ/β .

This quadratic temporal phase variation, or chirp, can be related to the phase front curvature by considering the input profile written in terms of the ‘complex beam parameter’, q , frequently used in the analysis of Gaussian beams [54],[55]. The spatial profile of the input beam at the pixelation plane, assuming an open spatial window (i.e. no pixelation) can be written as:

$$e_{in}(x) \propto \exp\left(-j \frac{k x^2}{2 q_{in}}\right) \quad (3.35)$$

where the complex beam parameter, q , is given by

$$\frac{1}{q(z)} = \frac{1}{R(z)} - j \frac{\lambda_o}{\pi n w^2(z)} \quad (3.36)$$

The complex beam parameter just prior to being dispersed by the diffraction grating can be obtained by calculating the system transfer matrix for the imaging components (i.e. the ABCD matrix formalism):

$$\mathbf{H} = \begin{bmatrix} A & B \\ C & D \end{bmatrix} \quad (3.37)$$

and applying the relation:

$$\frac{1}{q} = \frac{C + \frac{D}{q_{in}}}{A + \frac{B}{q_{in}}} \quad (3.38)$$

The imaging system transfer matrix can be formed from just two fundamental matrices: the propagation matrix over a distance L

$$\mathbf{L} = \begin{bmatrix} 1 & L \\ 0 & 1 \end{bmatrix} \quad (3.39)$$

and the lens matrix with focal length f

$$\mathbf{F} = \begin{bmatrix} 1 & 0 \\ -1 & 1 \\ f & 1 \end{bmatrix} \quad (3.40)$$

Using these two fundamental matrices, the imaging system transfer matrix is given by

$$\mathbf{H} = \mathbf{L}_{d2I} \mathbf{F}_{f2} \mathbf{L}_{d2O} \mathbf{L}_{d1I} \mathbf{F}_{f1} \mathbf{L}_{d1O} \quad (3.41)$$

where the subscripts indicate the value used in the fundamental matrix, $d1O$ is the distance from the pixelation plane to the first lens (an Object distance), $f1$ is the focal length of the first lens, $d1I$ is the distance from the first lens to the 'modulation plane' (an Image distance), $d2O$ is the distance from the 'modulation plane' to the second lens, $f2$ is the focal length of the second lens, and $d2I$ is the distance from the second lens to the diffraction grating.

It is possible to simplify the imaging system transfer matrix by realizing (and verifying experimentally by viewing with a CCD camera) that a good quality image is formed both at the modulation plane and at the grating shown in Fig. 3.6. Under this condition, the distance from the first lens to the 'modulation plane', $d1I$, and from the 'modulation plane' to second lens, $d2O$, may be expressed in terms of the focal lengths of the two lenses ($f1$ and $f2$), and the other two distances ($d1O$ and $d2I$) using the lens-makers formula:

$$\begin{aligned} \frac{1}{d1I} &= \frac{1}{f1} - \frac{1}{d1O} \\ \frac{1}{d2O} &= \frac{1}{f2} - \frac{1}{d2I} \end{aligned} \quad (3.42)$$

The imaging system transfer matrix is finally given by:

$$\mathbf{H} = \begin{bmatrix} \frac{f1(f2 - d2I)}{f2(f1 - d1O)} & 0 \\ \frac{(f2 - d2I)f1^2 + (f1 - d1O)f2^2}{f1f2(f2 - d2I)(f1 - d1O)} & \frac{f2(f1 - d1O)}{f1(f2 - d2I)} \end{bmatrix} \quad (3.43)$$

If the input beam at the pixelation mask is assumed to be well collimated ($R_{in} = \infty$), the complex beam parameter at the pixelation mask is purely imaginary and hence the beam parameter at the grating may be written in terms of the components of the imaging system transfer matrix:

$$\frac{1}{q} = \frac{C}{A} - j \frac{D}{A} \frac{\lambda}{\pi n w_{in}^2} \quad (3.44)$$

The phase front radius of curvature at the diffraction grating is then given by

$$\frac{1}{R} = - \frac{(f2 - d2I)f1^2 + (f1 - d1O)f2^2}{f1^2(f2 - d2I)^2} \quad (3.45)$$

and the beam size at the grating is given by

$$w^2 = \frac{f1^2(f2 - d2I)^2}{f2^2(f1 - d1O)^2} w_{in}^2 \quad (3.46)$$

Eqn. (3.45) and (3.46) can be used with (3.34) to calculate the chirp on the output of the DST pulse shaper due to the geometry of the imaging system optics.

3.3.1 Chirp measurement

In order to measure the chirp on the output of the DST pulse shaper, the pixelation mask is replaced by a single slit. As in Fig. 3.8, a single output pulse is generated from the DST shaper with this pixelation mask. The width of the pixelation mask is chosen as a trade-off between the output pulse width, and the width of the power spectrum at the

apparatus output. Fig. 3.12 shows results of the chirp measurement. The pixelation mask is translated across the input beam, and intensity cross correlations and power spectra are recorded as a function of pixelation mask position. The center wavelengths of the measured power spectra are plotted as a function of the time delays corresponding to each of the transverse pixelation mask positions. The slopes of the two curves in Fig. 3.12 are measures of the DST chirps for different imaging system magnifications. The slopes are 6.4 ps/nm and 6.8 ps/nm for imaging system magnifications of 4.2 and 6.5 respectively.

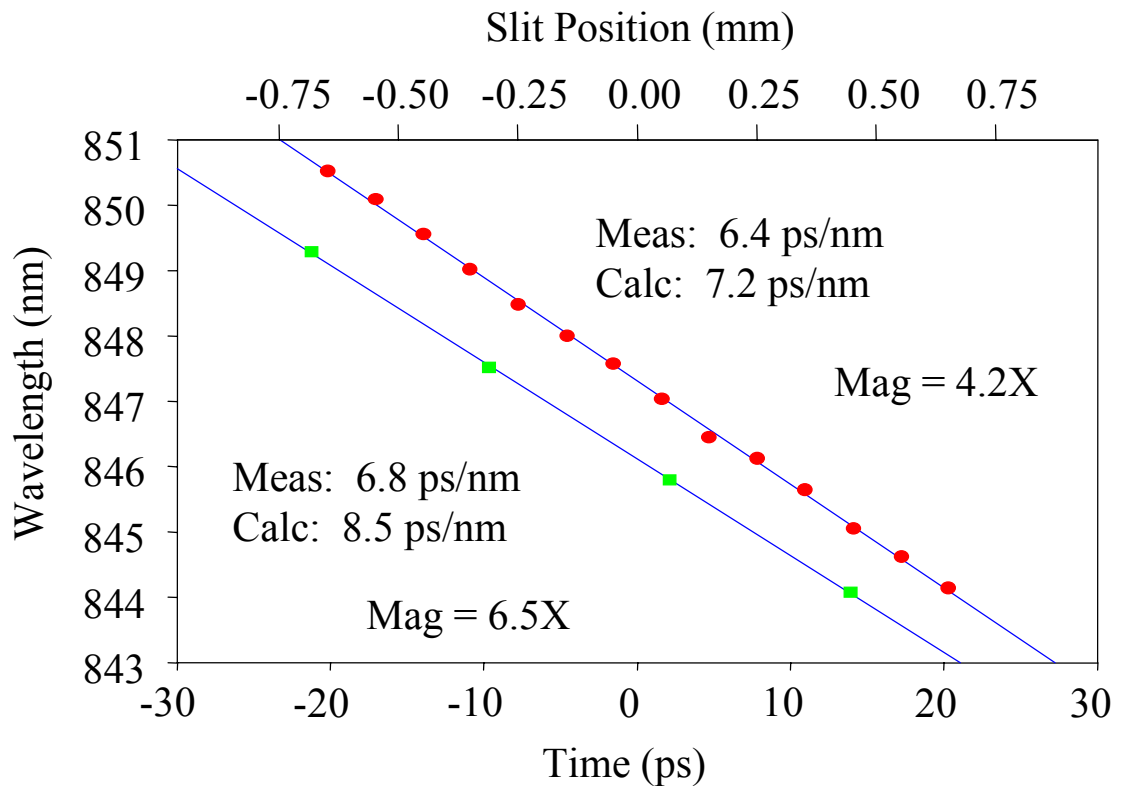


Fig. 3.12. Shift in output center wavelength as a function of input pixelation slit position (in space and time). The slope provides a measure of the chirp on the output of the DST pulse shaper.

A theoretical estimate of the expected chirp on the DST output can be obtained by numerically propagating a beam through the imaging system optics using Gaussian beam methods (ABCD matrices) [54][55] in order to determine an expected phase front

curvature at the surface of the diffraction grating as discussed in the previous section. Assuming a flat phase front at the surface of the pixelation mask, estimated values of chirp are 7.2 ps/nm and 8.5 ps/nm for imaging system magnifications of 4.2 and 6.5 respectively, which are in reasonable agreement with the experimental values. The difference between the measured and calculated chirps is due to the fact that the phase front is not completely flat at the pixelation mask.

3.3.2 Diffraction analysis

If the DST apparatus is to be used in optical communications applications, it will usually be necessary to control the chirp, and possibly set it to zero. One way to eliminate the chirp in the DST apparatus would be to utilize a telescopic configuration for relaying the masked spatial profile from the apparatus input to the diffraction grating. However, a flat phase front would be present at the diffraction grating only if a perfectly collimated (or focused) beam were present at the apparatus input with a precisely positioned telescopic configuration. Since these strict requirements may be undesirable in some cases, it is useful to explore alternative methods for eliminating the final term of Eqn. (3.24).

To this end we have performed a diffraction analysis of the DST apparatus [37]. Similar analyses have been previously performed for pulse stretchers [49] and pulse shapers [50]. In [37] we showed that changing the pulse shaping lens – output slit separation introduces a quadratic temporal phase term (chirp) to the output field that can be used to cancel the chirp resulting from the phase front curvature present at the

diffraction grating. In the following, we generalize the diffraction analysis in order to permit both the grating-lens and lens-slit separations to vary.

Fig. 3.13 shows a schematic representation of the different propagation regions included in the diffraction analysis. The grating-lens and lens-slit separations are denoted

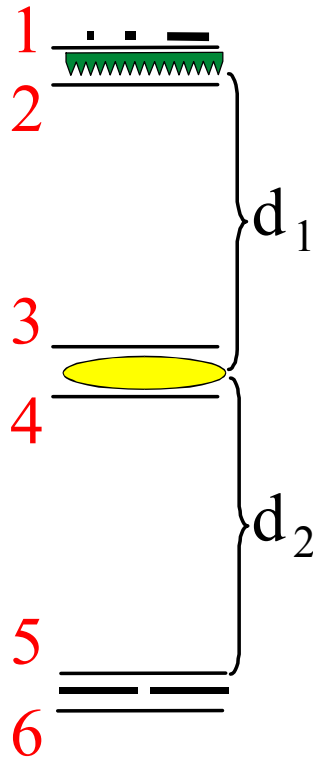


Fig. 3.13. Relevant planes considered in the diffraction analysis

d_1 and d_2 respectively. Following a procedure similar to [49] and [50], and starting with Eqn. (3.3), the spectral amplitude of the field just after the diffraction grating is written

$$E_2(x, \omega) \propto s(\beta x) \exp[-j \gamma \omega x] E_{in}(\omega) \quad (3.47)$$

The field just after the grating is propagated in the Fresnel regime to just before the pulse shaping lens [51], giving the following new expression for the spectral amplitude:

$$E_3(x, \omega) \propto \int_{-\infty}^{\infty} dx_2 E_2(x_2, \omega) \exp\left[\frac{j k}{2 d_1} x_2^2\right] \exp\left[\frac{-j k}{d_1} x_2 x\right] \quad (3.48)$$

Then the effect of the lens is included:

$$E_4(x, \omega) = E_3(x, \omega) \exp\left[\frac{-j k}{2 f} x^2\right] \quad (3.49)$$

followed by another propagation in the Fresnel regime to the output slit:

$$E_5(x, \omega) \propto \int_{-\infty}^{\infty} dx_4 E_4(x_4, \omega) \exp\left[\frac{j k}{2 d_2} x_4^2\right] \exp\left[\frac{-j k}{d_2} x_4 x\right] \quad (3.50)$$

Finally the effect of a delta-function output slit is included:

$$E_6(x, \omega) = E_5(x, \omega) \delta(x) \quad (3.51)$$

In order to relate the input and output fields, equations (3.47)-(3.51) are combined with Eqn. (3.10) for $s(x)$ and the identity [56]

$$\int_{-\infty}^{\infty} dx \exp\left[j(\alpha x^2 + \xi x)\right] = \sqrt{\frac{j \pi}{\alpha}} \exp\left[\frac{-j \xi^2}{4 \alpha}\right] \quad (3.52)$$

After considerable manipulation (shown in the appendix for reference), we obtain the result

$$e_{out}(t) \propto e_{in}(t) * \left\{N(t) \exp[-j \phi(t)]\right\} \quad (3.53)$$

where

$$N(t) = m \left(\frac{-\beta t}{\gamma} \right) \exp\left[\frac{-\beta^2 t^2}{\gamma^2 w^2}\right] \quad (3.54)$$

determines the temporal intensity profile of the output, and

$$\phi(t) = \frac{k}{2 \gamma^2} \left(\frac{\beta^2}{R} - \frac{d_2 - f}{d_1 f + d_2 f - d_1 d_2} \right) t^2 \quad (3.55)$$

gives the quadratic temporal phase and hence the chirp. The output chirp can be manipulated (in a special case compensated or set to zero) by varying d_1 and d_2 . The intensity profile and space-to-time conversion constant are expected to remain invariant as the chirp is manipulated in this way.

Unlike the well known grating and lens pulse stretcher [49], the chirp is most strongly affected by the lens-slit separation (d_2). When d_2 is fixed at the focal length of the lens ($d_2 = f$), output chirp is independent of the diffraction grating – lens separation, d_1 . Further, for bandwidth limited input pulses, the measured chirp in the $d_2 = f$ case can provide a measure of the phase front curvature at the surface of the diffraction grating, R . After determining the value of R in this way, the chirp can be calculated as a function of d_1 and d_2 with no further adjustable parameters using Eqn. (3.33) with Γ_i replaced by

$$\Gamma_i = \frac{k}{2\gamma^2} \left(\frac{\beta^2}{R} - \frac{d_2 - f}{d_1 f + d_2 f - d_1 d_2} \right) \quad (3.56)$$

The output chirp can be set to zero by adjusting d_1 and d_2 to achieve $\Gamma_i = 0$ (again assuming unchirped input pulses). It is interesting to note that in the case of a converging or diverging input beam at the grating (i.e., $R \neq \infty$), the beam is brought to a focus at a position other than the back focal plane of the lens. By using ABCD matrices, one can show that for d_1 and d_2 yielding $\Gamma_i = 0$, an input Gaussian beam with phase front radius of curvature R is brought to focus at exactly the position of the pulse shaping slit. This treatment is similar to the one performed at the end of section 3.3 where the transfer matrix for the pulse shaping components is given by

$$\mathbf{T} = \mathbf{L}_{d_2} \mathbf{F}_f \mathbf{L}_{d_1} \begin{bmatrix} -1 & 0 \\ \beta & -\beta \\ 0 & -\beta \end{bmatrix} \quad (3.57)$$

where the final term of (3.57) results from the beam size change off the grating (i.e. astigmatism). Multiplying out the terms of (3.57) results in the final form of the transfer matrix for the pulse shaping components

$$\mathbf{T} = \begin{bmatrix} \frac{-1}{\beta} \left(1 - \frac{d_2}{f} \right) & -\beta \left(d_2 + d_1 \left(1 - \frac{d_2}{f} \right) \right) \\ \frac{1}{\beta f} & -\beta \left(1 - \frac{d_1}{f} \right) \end{bmatrix} \quad (3.58)$$

When the beam comes to a focus, the phase front is flat ($R_{\text{focus}} = \infty$); so, using (3.38) to find the complex beam parameter at the focus of the pulse shaping lens (and remembering that it is purely imaginary) allows us to find the position of the beam focus in terms of the input phase front curvature, R , and the geometrical factors. The final result is

$$\frac{1}{R} = \frac{d_2 - f}{\beta^2 (d_2 f + d_1 f - d_1 d_2)} \quad (3.59)$$

exactly as expected from (3.56).

3.3.3 Measurements

In order to verify the predictions made in the previous section, we have performed a series of chirp measurements. The predicted and measured chirp are compared, with the value of R at the diffraction grating determined from the measured chirp in the configuration $d_1 = d_2 = f$.

Fig. 3.14 shows the measured chirp, in nm/ps, and space-to-time conversion constant as a function of the deviation of the pulse shaping lens-slit separation, d_2 , away from the focal length of the pulse shaping lens. This data was recorded for the configuration where the diffraction grating-pulse shaping lens separation was fixed at the

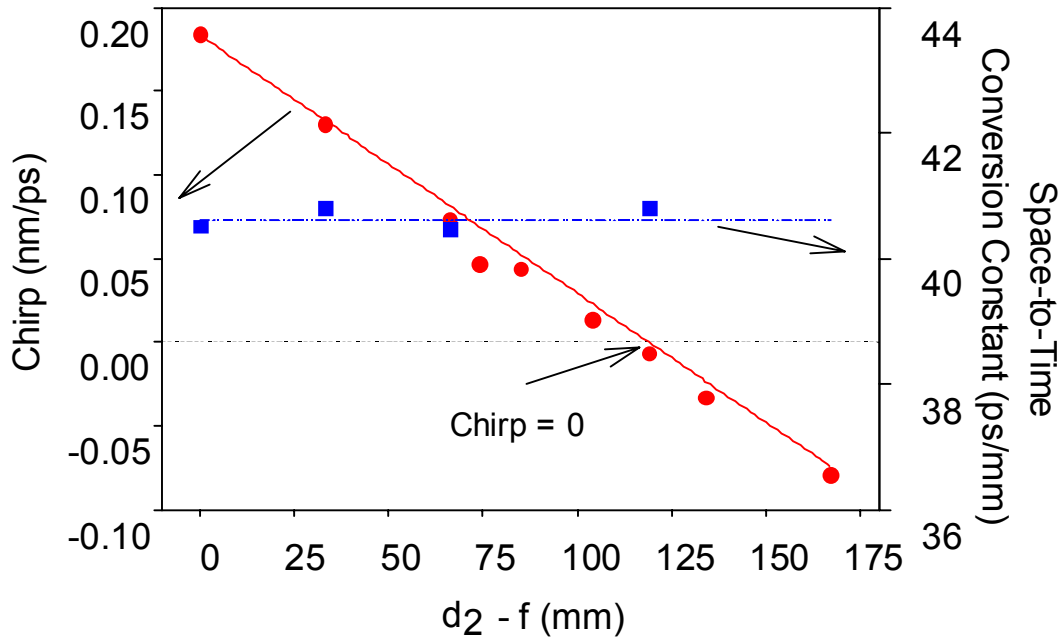


Fig. 3.14. Measured chirp and space-to-time conversion constant as a function of pulse shaping lens-output slit separation.

focal length of the lens ($d_1 = f$). The predicted and measured chirp are in excellent agreement over a large range of lens-slit separations. A chirp-free output is achieved for d_2 approximately 119 mm beyond the back focal plane of the lens. Further, the space-to-time conversion constant is observed to be flat as the chirp is varied over a wide range. This provides a first indication that the output intensity profile is invariant as the chirp is varied.

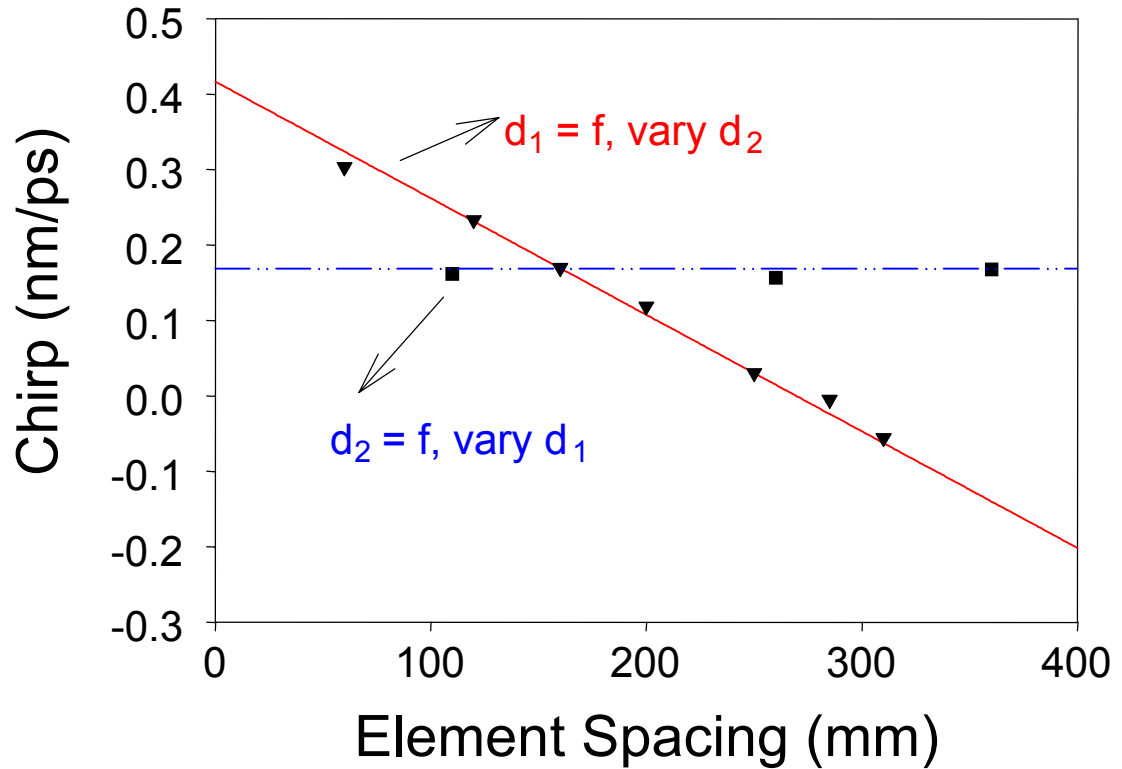


Fig. 3.15. Measured and calculated chirp for two interesting specific cases of the diffraction analysis result. Solid line is calculated and triangles are measured for grating-lens separation, $d_1 = f$, but lens-slit separation allowed to vary. Dashed line is calculated and squares are measured for lens-slit separation held fixed at the focal length of the pulse shaping lens while grating-lens separation is allowed to vary.

Fig. 3.15 shows the measured chirp in two special cases. In one case, the diffraction grating-pulse shaping lens separation, d_1 , is allowed to vary while the pulse shaping lens – output slit separation, d_2 , is fixed at the focal length of the lens, f . In the second case the converse is true, d_2 is varied while $d_1 = f$ is maintained. In the first case, the output chirp does not change with d_1 as expected from our prediction. The second case is data similar to that shown in Fig. 3.14, and is repeated just for reference.

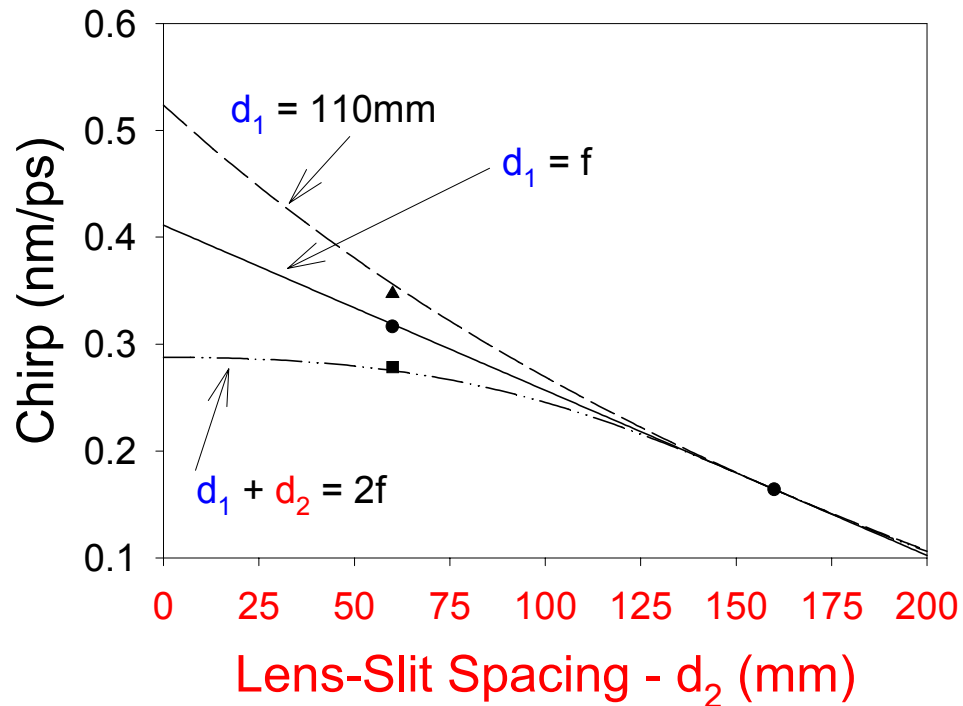


Fig. 3.16. Calculated (lines) and measured (symbols) chirp in the general case.

Two specific implementations of the general case (neither d_1 nor d_2 equal to f) are shown in Fig. 3.16, along with the special case of $d_1 = f$. In the top trace, the grating-lens separation is set to a fixed value of 110 mm (compared to $f = 160$ mm), and the predicted chirp is plotted as a function of the lens-slit separation, d_2 . In the bottom case, both d_1 and d_2 are varied, but their sum is held fixed at twice the focal length of the lens. Both of these new cases are tested by a chirp measurement at $d_2 = 60$ mm. In each case the calculated and measured chirp are in excellent agreement.

Finally, in order to verify that the output intensity profile is invariant as the chirp is adjusted, intensity cross correlation traces of an ultrafast data packet were recorded for three different amounts of output chirp. The results are shown in Fig. 3.17, and in all cases $d_1 = f$. The top trace was taken in a moderately chirped configuration when $d_2 = f$. The middle trace was taken in a partially compensated chirp configuration, $d_2 - f = 66$ mm, and the bottom trace was taken in a chirp-free configuration, $d_2 - f = 119$ mm. The general shape of each of the three cross correlation traces is the same verifying that the output intensity profile is unchanged as the chirp on the DST output is varied. The minor differences in the envelopes of the three traces is due to slight changes in the centering of the pixelation mask on the input beam from one measurement to the next.

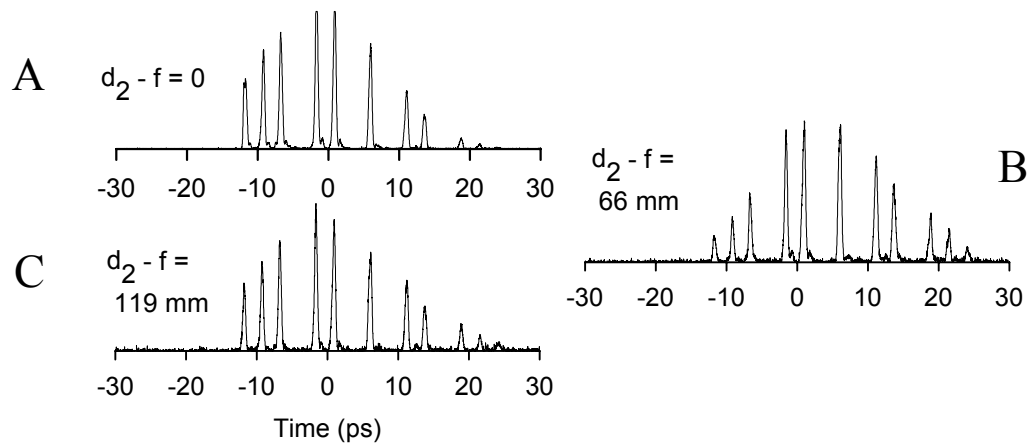


Fig. 3.17. Intensity cross correlation measurements of the DST pulse shaper output for an 'optical packet' pixelation mask, and three values of output chirp. (A) is heavily chirped, (B) moderately, and (C) approximately chirp-free.

3.4 Multiple Output Channels

In all the discussions thus far, a single output slit has been assumed, with the implication is that this slit is centered on the dispersed frequency spectrum. Specifically, the ideal output slit was taken to be positioned at an arbitrary, but convenient position, $x = 0$. As we shall see any other transverse position of the output slit yields exactly the same intensity profile as eqn. (3.8), but with a wavelength shift. In fact, a multiple element slit could be used instead of the single slit resulting in multiple spatially separated output beams. This section will focus on the output multiple wavelength nature of the DST apparatus.

3.4.1 Mathematical description

The multiple output nature of the DST apparatus follows directly from the previous discussions of the space-time mapping. In the following, for convenience, the DST apparatus is assumed to be configured chirp-free. That is, the pulse shaping lens – output slit separation, d_2 , is set to cancel the quadratic temporal phase term due to the phase front radius of curvature at the diffraction grating. However, the important features derived below also hold for the more general case where the chirp is not compensated. In the chirp-free case, the spatial profile mapped to the time domain consists of just the first two terms of eqn. (3.10) – the masking function, and the beam profile:

$$s(x) = m(x) \exp\left[\frac{-x^2}{w^2}\right] \quad (3.60)$$

The complex spectrum just prior to the output slit(s) is given by:

$$E_3(x, \omega) \propto S\left(\frac{2\pi x}{\beta\lambda f} - \frac{\gamma\omega}{\beta}\right) E_{in}(\omega) \quad (3.61)$$

Consider now a thin slit at lateral position x_s , i.e., of the form $\delta(x-x_s)$. The filtered spectrum now has the form

$$E_4(x, \omega) \propto S\left(\frac{2\pi x}{\beta\lambda f} - \frac{\gamma\omega}{\beta}\right) E_{in}(\omega) \delta(x - x_s) \quad (3.62)$$

Note that $S(\dots)$ is the spectral response function of the generalized spectrometer. eqn. (3.62) shows that a transverse movement of the output slit leads to a simple shift in the spectral response function of the DST pulse shaper, just as it would in an ordinary spectrometer, even though the spectral response of the DST may be much more complex than that of a spectrometer.

The time domain response corresponding to eqn. (3.62) is given by

$$e_{out}(t) \propto e_{in}(t) * \left\{ s\left(\frac{-\beta t}{\gamma}\right) \exp\left[\frac{j 2\pi x_s}{\gamma\lambda f} t\right] \right\} \quad (3.63)$$

The impulse response function is given by the terms inside the $\{\dots\}$ sign and consists of two terms. The first, $s(-\beta t/\gamma)$, represents the space-to-time conversion constant and is unchanged compared to our earlier treatment. The second, linear phase term represents a frequency shift. Thus, a lateral movement of the output slit tunes the output optical frequency while leaving the intensity profile of the shaped output waveform unaffected.

We can also consider a multiple output slit element which spatially separates each output beam in a non-overlapping manner. The output from each independent slit is still given by equations (3.62) and (3.63), with the appropriate slit position inserted for x_s . Thus, the DST pulse shaper should be able to simultaneously generate multiple spatially separated, wavelength shifted outputs, each with the identical intensity profile. In cases

where such multiple outputs are useful, this increases the overall optical efficiency by a factor equal to the number of outputs.

3.4.2 Measurements

In order to demonstrate the shift in output center wavelength as a function of transverse output slit position, a periodic pixelation mask consisting of 20 transparent rectangles in an otherwise opaque background was inserted into the pixelation plane of the DST pulse shaper. As shown previously, use of this pixelation mask will result in a temporal output intensity profile that is a train of pulses. Accordingly, one expects this output temporal profile to correspond to a periodically modulated power spectrum after the output slit. Fig. 3.18 shows a series of nine power spectra recorded at periodic

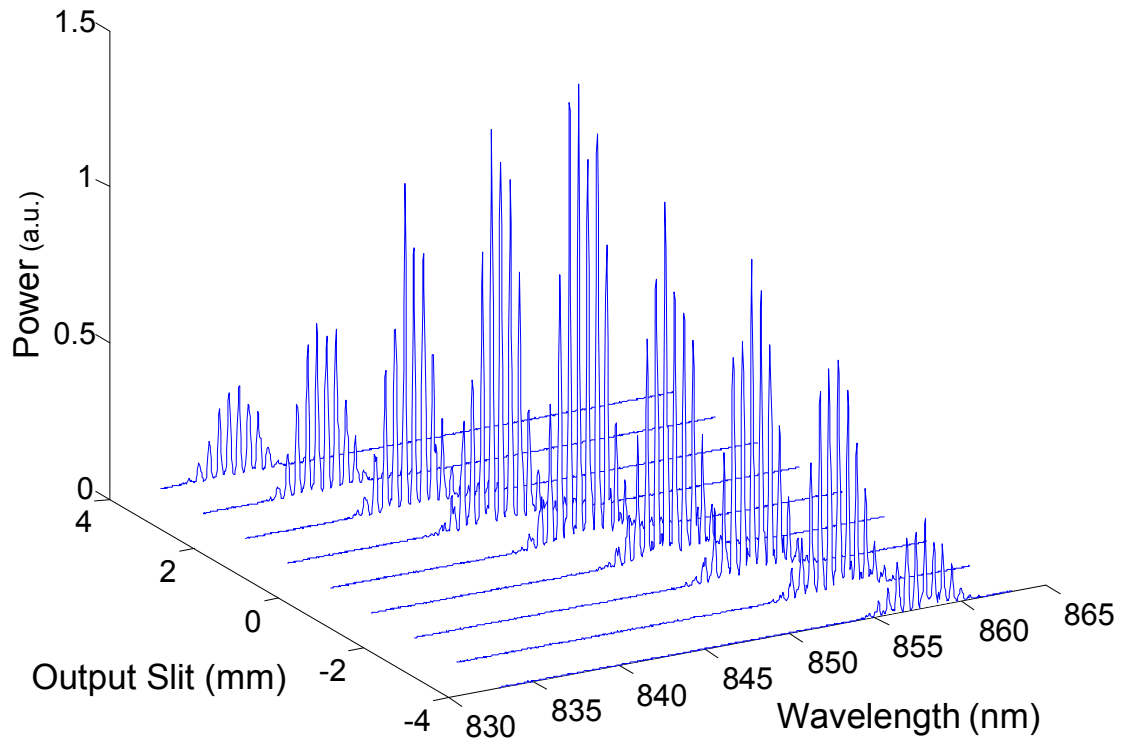


Fig. 3.18. Output power spectra as a function of transverse pulse shaping slit position for a periodic pixelation mask.

transverse output slit positions separated by 1 mm. The trend of a shift in center wavelength as a function of transverse output slit position is quite evident when plotted in this manner. Further, Fig. 3.18 shows that multiple spatially separated output channels could be generated by replacing the single output slit used in these measurements with a multiple element slit.

The invariant shape of the output power spectra in Fig. 3.18 imply that the temporal profile of each output is invariant as well. Further evidence of this assertion is shown in Fig. 3.19. Here, intensity cross correlation traces are shown for two different output slit positions separated by 2 mm transverse distance as well as two different

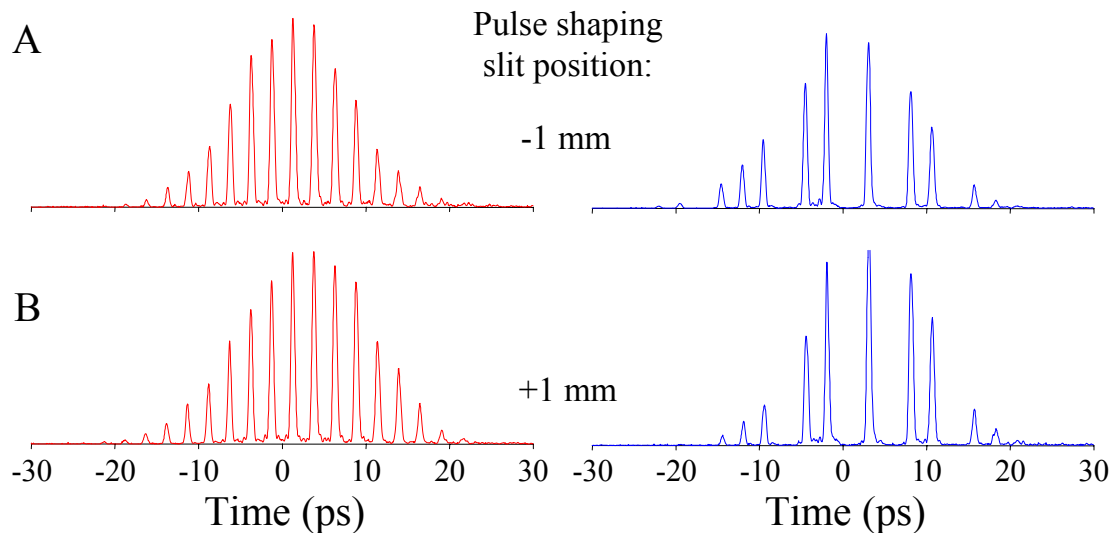


Fig. 3.19. Intensity cross correlation measurements of the DST pulse shaper output for two different transverse positions of the pulse shaping slit separated by 2 mm.

pixelation mask patterns. The 2 mm transverse distance between the output slit positions corresponds to a 3.6 nm shift in the center wavelength of the output power spectra. The left two traces correspond to the pixelation mask used to measure the power spectra shown in Fig. 3.18 – a periodic 20 pixel ‘pulse train’ mask. The right two traces correspond to a ‘data packet’ mask similar to the mask used for the data presented in Fig.

3.10. These four cross correlation's clearly shown the invariant nature of the output temporal intensity profile as expected from Eqn. (3.63) and the recorded power spectra.

3.5 Summary of DST / FT Differences

The major differences between the FT pulse shaper described briefly in chapter 2 and the DST pulse shaper described above in detail will be summarized here. First, it is important to remember that both the FT and DST pulse shapers are capable of generating highly complex output waveforms. The selection of which pulse shaping geometry to employ for a specific application therefore need not be dominated by concern for pulse shape fidelity; rather, the relative difficulty of implementing the masking function in either geometry should be considered along with optical power throughput considerations. The major differences between the two pulse shaping geometries are shown in the following table.

Table 3.1
Differences between the FT and DST pulse shapers.

	FT	DST
Difference between spatially patterned mask, $m(x)$, and the output temporal profile.	$e_{\text{out}}(t) \propto \mathfrak{F}\{m\}$	$e_{\text{out}}(t) \propto m$
Chirp	$\exp(-j \phi \omega^2)$ Adjust with grating-lens separation.	$\exp(-j \phi t^2)$ Adjust with lens-slit separation.
Efficiency for pulse train generation (N pulses) with amplitude mask.	$\sim N t_p / T$	$\sim t_p / T$ (single output channel)
Multiple output channels?	No	Yes

As the names imply, the FT pulse shaping geometry has a Fourier transform relationship between the output temporal profile and the masking function while the DST pulse shaper has a direct scaling between the masking function and the output temporal profile. The character of the chirp present at the apparatus output can be a source of confusion for these configurations. Simply stated, the space-time mapping of the DST pulse shaper results in a quadratic temporal phase variation on the output due to a finite phase front radius of curvature at the diffraction grating. As was shown previously, this chirp can be manipulated by varying the geometry of the apparatus, and the primary geometrical factor that impacts the chirp is the pulse shaping lens – output slit separation. The FT shaper, as commonly used in pulse stretchers, has a quadratic spectral phase variation on the output that is manipulated by varying the separation between the diffraction grating and the lens. In this discussion, both the quadratic temporal phase (DST) and spectral phase (FT) have been referred to as a chirp. These two quadratic phase variations are only strictly equivalent when a Gaussian (temporal) input pulse is utilized.

The efficiency of pulse train generation in the DST pulse shaper was discussed above, and was shown to be roughly pattern independent provided that the pixelation function of the mask is carried out in an energy conservative manner. When the FT pulse shaper is used, with amplitude filtering only, to generate a single output pulse of duration T from an input pulse of duration t_p , the efficiency is approximately t_p/T . When a pulse train is generated with amplitude filtering alone in the FT pulse shaper, the efficiency is then approximately $N t_p/T$ where N is the number of pulses in the output pulse train. This means that the FT shaper has approximately N times greater output power than the DST

pulse shaper under these conditions. However, it is possible to obtain multiple spatially separated outputs from the DST pulse shaper while it is not possible in the FT geometry. If the application requires multiple output channels with identical temporal intensity output profiles, the efficiency of the DST pulse shaper and the FT pulse shaper (with amplitude masking) could then be approximately equal.

4. INTEGRATED OPTIC CONFIGURATION

The bulk optics implementation of the DST pulse shaper explored in the previous chapter provides a background through which it is possible to realize the same functionality of the bulk optics apparatus in an integrated optic configuration. The integrated optic configuration provides a significant savings in physical footprint when compared to the current embodiment of the bulk optics DST pulse shaper as shown in Fig. 4.1. This new implementation of the DST pulse shaper is based on a modified Arrayed-Waveguide Grating (AWG) structure – a device that has seen considerable use in high-speed photonic networks primarily as Wavelength-Division Multiplexed (WDM) multiplexers and demultiplexers. After reviewing the conventional use of AWG devices as WDM channel filters, this chapter will explore two configurations of AWG-based

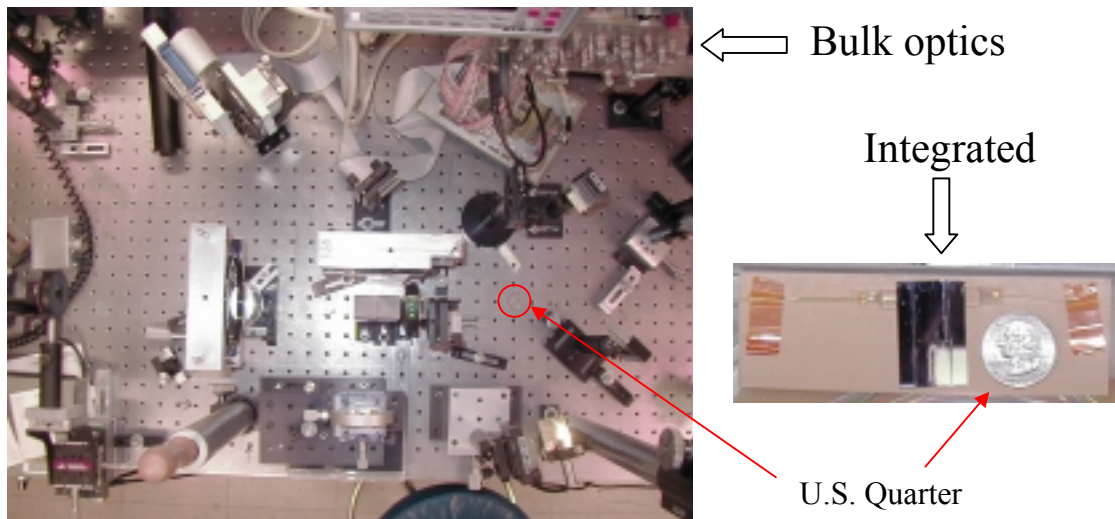


Fig. 4.1. Photos of the bulk optics DST pulse shaper (left) and an AWG (right).

devices. One configuration yields trains of very-high repetition rate pulses, and the other configuration may useful for more general DST pulse shaping.

4.1 Background

The typical AWG, shown schematically in Fig. 4.2 [39],[40],[57], is a planar waveguide structure fabricated by the flame-hydrolysis deposition of glass onto a silicon substrate. Conventional microlithographic techniques are used to form the planar lightwave circuit along with reactive-ion etching. The typical AWG consists of three regions – an input and output waveguide or waveguides, input and output slab waveguides, and a waveguide array. Light is typically coupled into the device from a

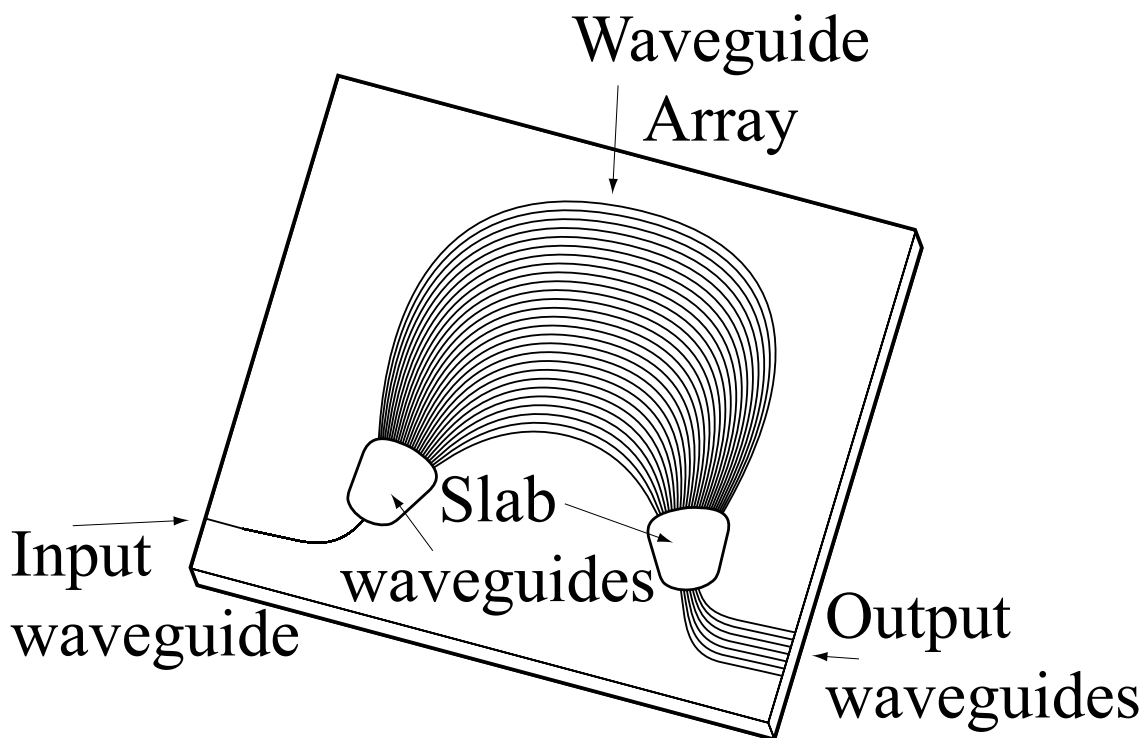


Fig. 4.2. AWG Structure.

fiber (or fibers) connected to the input guide (or guides). The light in the input slab waveguide is not as strongly confined (in one dimension) as in the input guide; so, the light out of the input guide diverges in the input slab in order to excite the guides of the waveguide array. The excitation intensity of the light in the guides of the waveguide array typically follows a Gaussian distribution due to the divergence in the input slab waveguide. The guides that make up the waveguide array have a constant length difference between adjacent guides in the array, ΔL , and this length difference is designed to be some integer multiple of the design center wavelength of the device. The output of the waveguide array can then be considered to be a phased array of emitters. The beams from each element of the waveguide array constructively interfere at the output guides with the position of constructive interference being wavelength dependent due to the phase shift across the waveguide array. Wavelength dependent output channels are obtained by positioning the spatially separated output guides along the dispersed spectrum out of the waveguide array. The output edges of the waveguide array, and the edges of the output guides are configured along a curved surface similar to a Rowland circle spectrograph in order to minimize wavelength dependent aberrations [57],[58].

The wavelength dependent filter functionality described above for the AWG has seen considerable development in the past few years [39],[40] primarily in the development of devices for use as WDM channel demultiplexers and routers in optical networks. In contrast AWG devices have seen only limited use in time domain applications. For example, modelocked pulse inputs have been spectrally sliced to yield pulses in the tens of picoseconds range at the repetition rate of the modelocked source

laser [59], and supercontinuum sources have been sliced to yield multiple optical wavelengths for high-speed systems studies [47],[60]. Modified AWG devices have also been used for Fourier transform optical pulse shaping [21]. Here we present a completely new functionality, in which the AWG produces bursts of femtosecond pulses repeating at a THz rate, with the pulse repetition rate determined by the AWG design rather than the input pulse repetition rate. Furthermore, wavelength shifted but otherwise identical femtosecond pulse bursts are obtained at different output channels of the AWG, very much like the direct space-to-time (DST) pulse shaper previously investigated only in bulk optics [22]-[38],[41],[42].

Perhaps this new functionality has thus far gone unrealized by the many users of AWG devices due to their concentration on the spectral response of the devices and the primary use in traditional WDM networks. Background in ultrafast optics, and an understanding of the importance of both spectral and temporal responses lead to a realization of the potential for modified AWG devices to fulfill the same space-time mapping and multiple spatially separated but wavelength shifted outputs as the bulk optics DST pulse shaper. Fig. 4.3 demonstrates the primary design issue in AWG devices that impacts their use with short optical pulses. Typical WDM network designers require that the free-spectral range (FSR) of the AWG filters be large compared to the total channel frequency span in the WDM network as demonstrated in Fig. 4.3A. This requirement comes about in order to ensure that only a single specific, known output wavelength is present at each output of the AWG. If the AWG is designed to the opposite extreme, as shown in Fig. 4.3B, where the FSR is small compared to the bandwidth of the source laser used with the device, the space-time mapping becomes

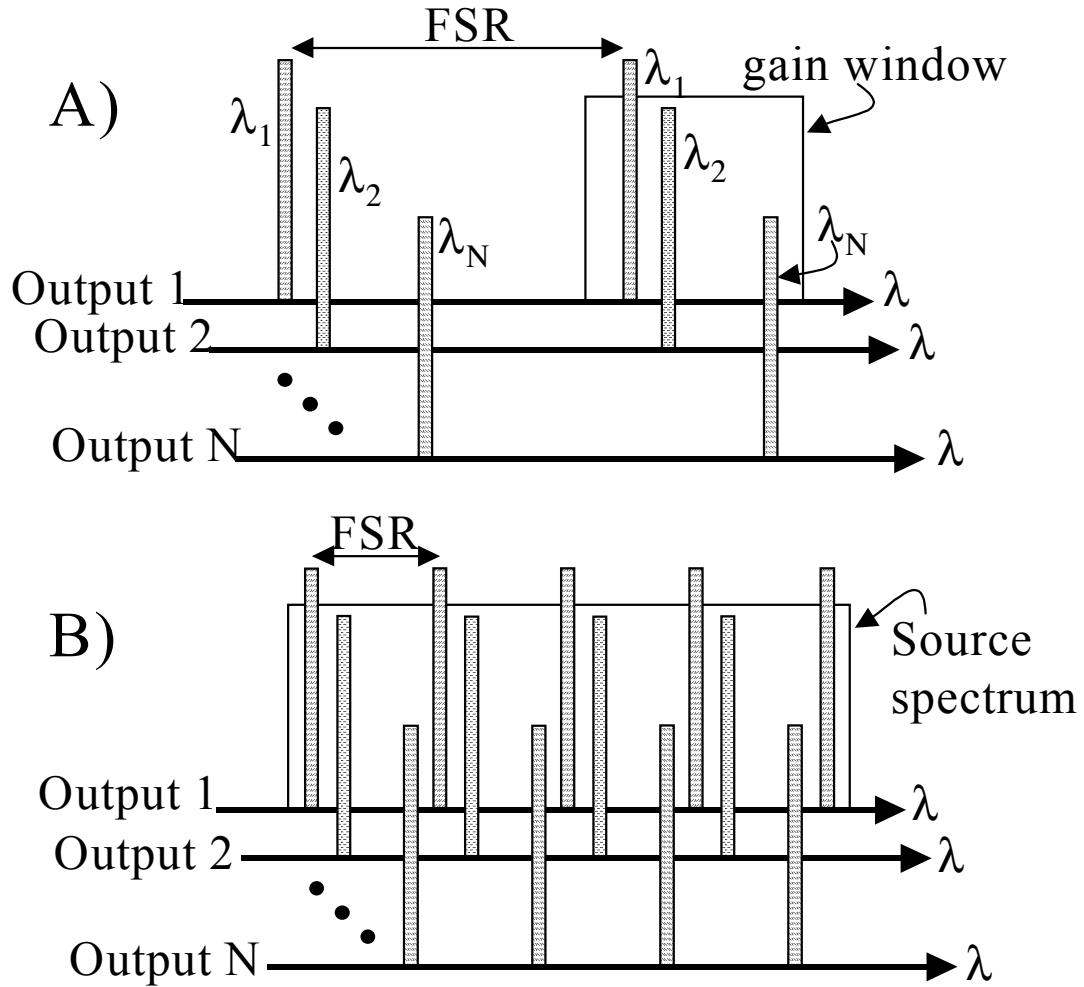


Fig. 4.3. Filter design methodologies for (A) traditional AWG filters, and (B) DST pulse shaping using an AWG.

evident. Conversely, this means that the bandwidth limited input pulse width, t_p , is less than the delay increment per guide, $\Delta\tau$, in the waveguide array. The time domain output then consists of a train of pulses with pulse separation, $\Delta\tau$, equal to the waveguide array delay increment. The duration of the individual output pulses is the same as the input pulse, and the duration of the envelope of the pulse train varies inversely with the AWG passband width. The 'one guide – one pulse' methodology is helpful in understanding the general space-time mapping of these devices.

4.2 DST / AWG Analogy

From the perspective of the DST pulse shaper of Fig. 3.13, the waveguide array in Fig. 4.2 can be viewed as equivalent to a curved diffraction grating. This is analogous to the grating/lens combination of the DST with $d_1 = 0$. The output waveguides of the AWG are analogous to a multiple element output slit in the DST pulse shaper. The waveguide array – output slit separation is equal to the focal length for light emerging from the waveguide array; therefore $d_2 = f$. The spatially modulated field pattern at the output of the waveguide array section is equivalent to a periodically modulated spatial pattern in the DST. By analogy, under appropriate conditions, an AWG read out by a femtosecond pulse should lead to a very high repetition rate femtosecond pulse train. The combination of the grating and lens into a single element does not modify the character of the output since we know from the work in the DST pulse shaper that the combination $d_1 = 0, d_2 = f$ does not introduce any chirp.

For short pulse applications, the important AWG parameter determining the character of the output is the free spectral range (FSR), which is equal to the inverse of the delay increment per guide ($\Delta\tau$):

$$\text{FSR} = \Delta\tau^{-1} = \frac{c}{n_{\text{eff}} \Delta L} \quad (4.1)$$

where n_{eff} is the effective index of the waveguide, c is the speed of light in vacuum, and ΔL is the physical path length difference from one guide to the next in the waveguide array section of the AWG. The key design constraint of the AWG is that the free spectral range (FSR) must be less than the optical bandwidth, $\Delta\nu$, of the source laser. In this case, the output spectrum of any single waveguide in the AWG is multiply peaked,

with the spectral peak spacing equal to the FSR. Conversely, this means that the bandwidth limited input pulse width, t_p , is less than the delay increment per guide, $\Delta\tau$, in the waveguide array. The time domain output then consists of a train of pulses with pulse separation, $\Delta\tau$, equal to the waveguide array delay increment. The duration of the individual output pulses is the same as the input pulse, and the duration of the envelope of the pulse train varies inversely with the AWG passband width. We note again that the requirement that $\text{FSR} < \Delta\nu$ is opposite to the normal usage in DWDM systems, where the free spectral range must exceed the range of wavelengths employed.

Alternatively, the pulse-to-pulse separation in the output pulse train burst can be calculated by viewing the AWG as an integrated version of a DST pulse shaper. Viewed this way, the pulse repetition period ΔT is given by:

$$\Delta T = a \left(\frac{\gamma}{\beta} \right)_{\text{AWG}} \quad (4.2)$$

where a is the pitch of the waveguide array at the interface of the waveguide array and output slab waveguide and $(\gamma/\beta)_{\text{AWG}}$ is the space to time conversion constant for the arrayed waveguide grating. γ in eqn. (4.2) is calculated according to eqn. (3.4) with $n = n_s$, the effective slab waveguide refractive index, and where $\frac{d\theta_d}{d\lambda}$ is expressed for the AWG as [61]:

$$\frac{d\theta_d}{d\lambda} = \frac{m n_g}{a n_s n_c} \quad (4.3)$$

The grating order, m , is given by

$$m = \frac{n_c \Delta L}{\lambda} \quad (4.4)$$

n_c is the effective index of the waveguide array, and n_g is the group index of the waveguide array, and λ is defined as the free space wavelength. The astigmatism parameter β is assumed to be 1, or $\theta_d \approx \theta_i \approx 0$ which is a reasonable assumption given typical dimensions of AWG devices. Therefore,

$$\left(\frac{\gamma}{\beta}\right)_{\text{AWG}} \approx \gamma_{\text{AWG}} = \frac{n_s \lambda}{c} \frac{n_c \Delta L}{\lambda} \frac{n_g}{a n_s n_c} = \frac{\Delta L n_g}{a c} \quad (4.5)$$

From eqn. (4.2), the pulse repetition period is given by

$$\Delta T = \frac{\Delta L n_g}{c} \quad (4.6)$$

This is exactly equal to the delay increment per waveguide, $\Delta\tau$, which is the expected pulse separation based on the earlier argument. This supports our view of the response of the AWG as analogous to that of the DST pulse shaper.

4.3 Pulse Train Generator

In the AWG experiments described here, a modelocked erbium fiber laser producing a 50 MHz train of ~200 fs pulses at 1560 nm is utilized. In principle, similar experiments can also be performed using much higher rate (e.g. >10 GHz) modelocked pulse sources. The AWG devices have a 1 THz FSR corresponding to a 1 ps delay increment per guide in the waveguide array. Two different devices were investigated, one having a 100 GHz output channel spacing and the other having a 40 GHz output channel spacing. A schematic diagram of the experimental apparatus is shown in Fig. 4.4. A 10/90 fiber splitter is used to generate reference and signal paths respectively with both fiber links constructed to be dispersion compensated using an appropriate

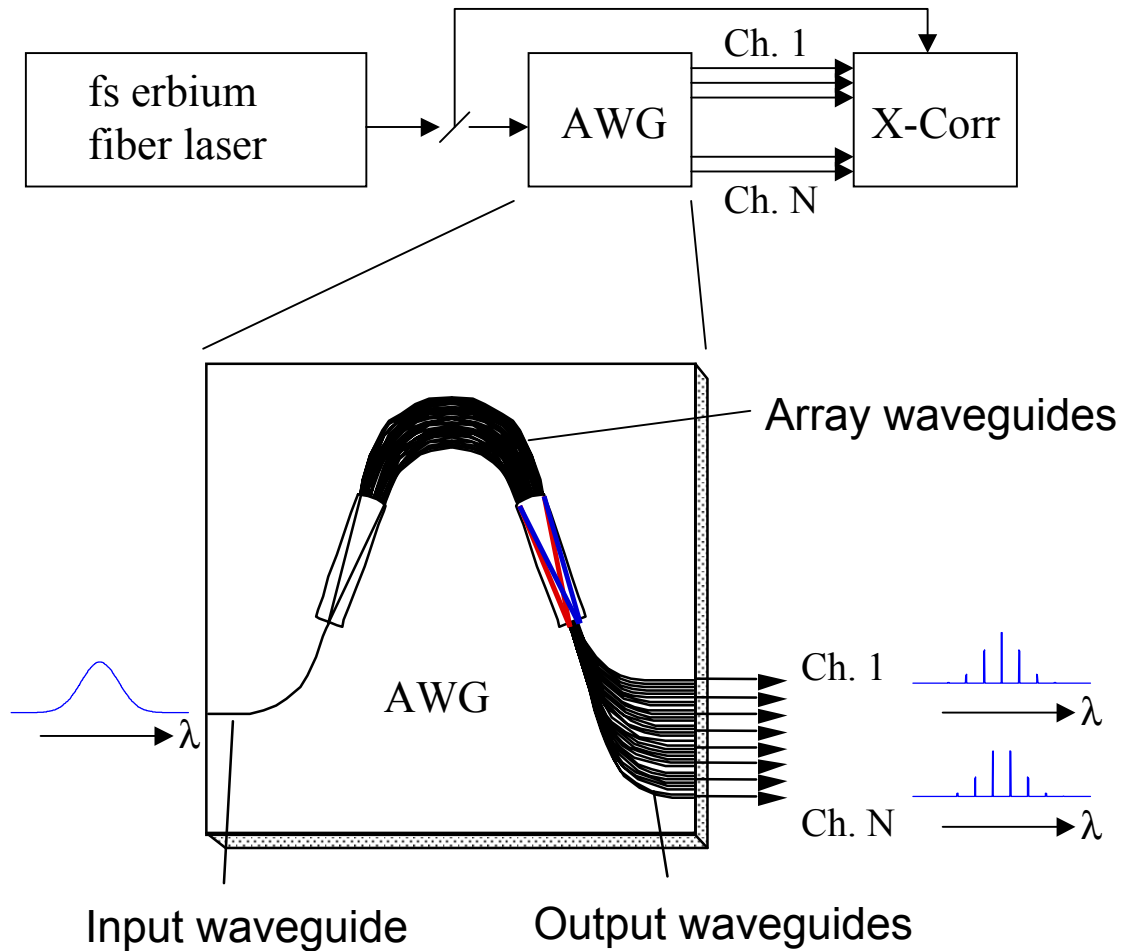


Fig. 4.4. Experimental apparatus for AWG pulse train generation experiments.

combination of single-mode fiber (SMF) and dispersion compensating fiber (DCF). The 90% arm is launched into the AWG under test, and the temporal profile of the output is measured by intensity cross correlation with the 10% reference port. The cross correlation apparatus utilizes a free-space delay stage to vary the time delay between the signal and reference paths, but is fiber coupled in order to simplify alignment. Power spectra of the device outputs are recorded as well with an optical spectrum analyzer.

For each AWG, separate dispersion compensated fiber links were constructed for both the signal and reference paths in order to ensure that the laser pulses out of the links

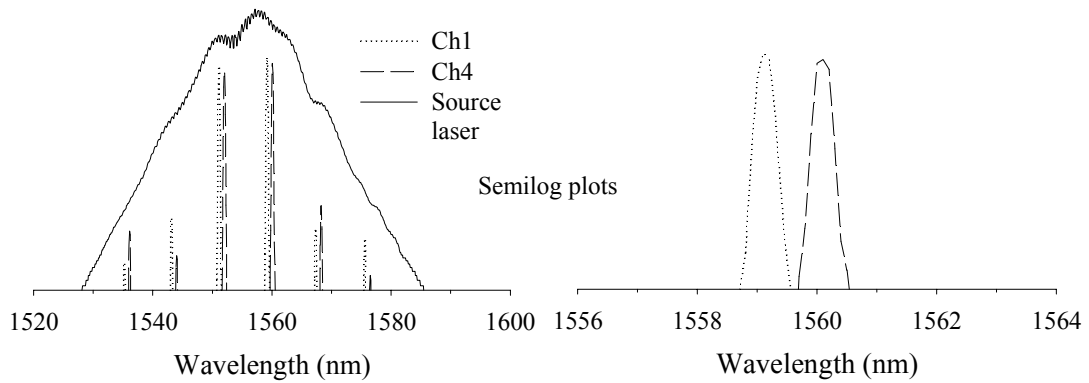


Fig. 4.5. Measured power spectra from the 40 GHz output channel spacing AWG. Both the full wavelength span (left) and the expanded (right) curves are plotted on a semi-log scale to more readily show the multiple filter passbands.

were not significantly broadened relative to the input pulses while simultaneously making sure that the optical path length of the signal and reference paths were nominally the same. The span of the free-space delay stage provided some measure of flexibility in adjusting the lengths of the fiber links; although, significant iteration was required to simultaneously keep the reference and signal links dispersion compensated while ensuring temporal overlap in the cross correlation apparatus.

Fig. 4.5 shows power spectra recorded from an AWG device with 40 GHz output channel spacing. The power spectrum of the source laser is overlaid with the output power spectra recorded from channels 1 and 4. The 1 THz FSR is evident from the periodic passband structure with 8.1 nm spacing between peaks. The spectra consist of six discrete output frequencies within the bandwidth of the source laser for each output channel. The shift in output center wavelength from one output to another is apparent as well. The multiply peaked nature of the power spectra demonstrate that $\Delta\nu > \text{FSR}$; therefore, the output temporal profile is expected to be a train of pulses where the temporal period of the pulses in the output train is given by the inverse of the FSR.

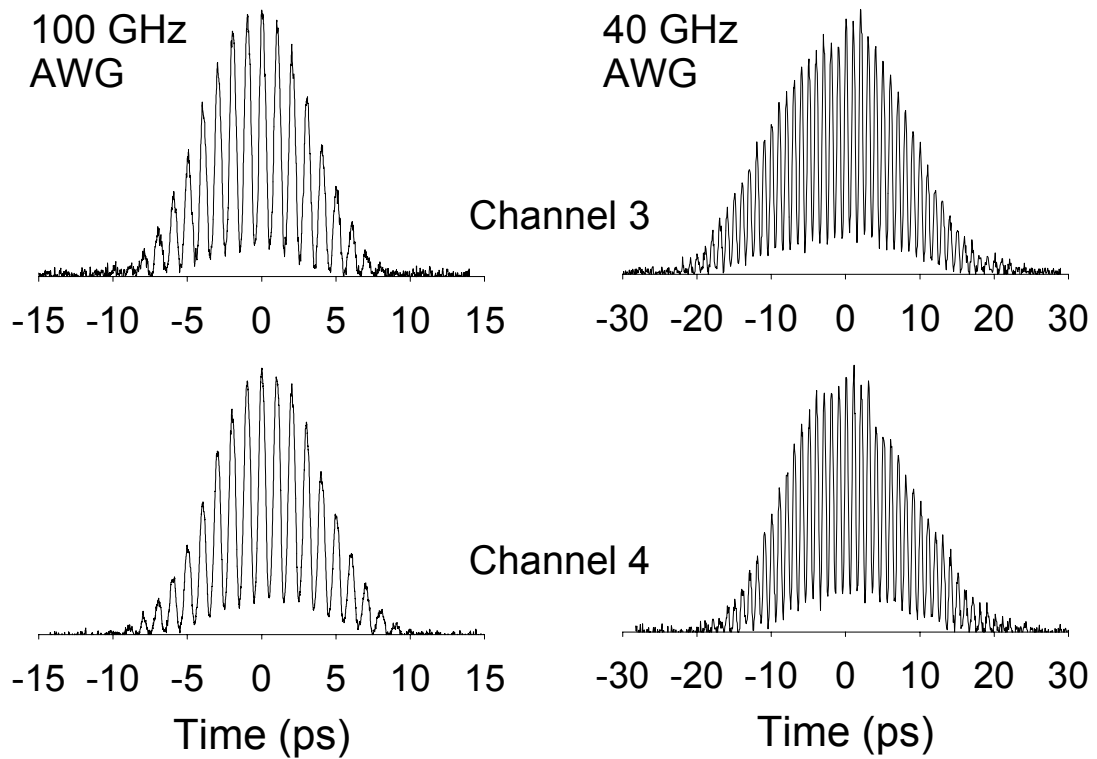


Fig. 4.6. Intensity cross correlation measurements of the 100 GHz output channel spacing (left) and 40 GHz output channel spacing (right) devices for output channels 3 (top) and 4 (bottom).

Fig. 4.6 shows intensity cross correlation measurements of two different AWG devices – the 40 GHz output channel spacing device used in the power spectra measurements of Fig. 4.5, and a 100 GHz output channel spacing device. As expected from the power spectrum presented above the temporal profile consists of a train of pulses with a 1 ps period, corresponding to the AWG delay increment, which is the inverse of the FSR, and with a pulse duration comparable to that of the input pulse. The temporal window (or number of pulses) is inversely proportional to the AWG filter bandwidth and therefore increases by 2.5 times from the 100 GHz device to the 40 GHz device. The form of the output intensity profile is the same for different output channels

of a single device, even though the spectrum is shifted, which is identical to the multiple wavelength nature of the bulk optics DST presented above.

In Fig. 4.7, the calculated pulse train envelope for the 100 GHz output channel spacing device is indicated by the dashed line. The envelope is calculated from a measurement of a single passband in the power spectrum. If the form of the passband is denoted as $|A(\omega)|^2$, the envelope, $|a(t)|^2$, is taken as

$$|a(t)|^2 = \left| \frac{1}{2\pi} \int d\omega \sqrt{|A(\omega)|^2} \exp(j\omega t) \right|^2 \quad (4.7)$$

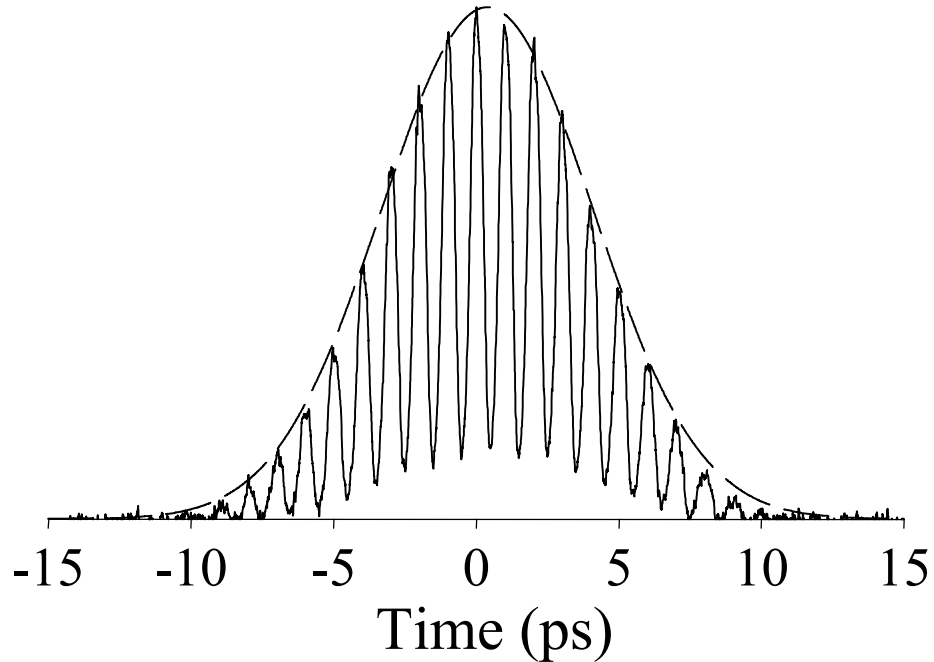


Fig. 4.7. Measured intensity cross correlation (solid) from the 100 GHz output channel spacing device overlaid with the calculated temporal window (dash).

The actual envelope indicated by the measured intensity cross correlation, shown by the solid line in Fig. 4.7, is in excellent agreement with this calculation confirming the inverse relationship between the AWG passband width and duration of the output pulse sequence.

To date, all the experimental work performed on these devices has been carried out using a low repetition rate (40 – 50 MHz), passively modelocked laser source producing pulses > 200 fs. Each pulse from the source laser generates a burst of very-high repetition rate pulses. In principle it should be possible to generate continuous trains of very-high repetition rate pulses (> 500 GHz) by utilizing an actively modelocked short pulse laser (10 – 20 GHz). When the repetition rate of the source laser is on the order of the output pulse burst duration, the output pulse bursts will combine to form a continuous or quasi-continuous output train, sometimes called 'rate multiplication' in the optical communications arena. This application and other potential uses for the high repetition rate pulse train generator will be discussed in chapter 5.

4.4 Integrated DST

The pulse train generator configuration of an AWG described above may be of interest for applications requiring multiple synchronized but spatially separated output channels consisting of bursts of very-high repetition rate pulses. However, more general functionality, in terms of allowing arbitrary pulse sequence generation, would increase its potential applicability even further. From our understanding of the bulk optics implementation of the DST pulse shaper, and the analogy between the DST and AWG presented in section 4.2, it is apparent that arbitrary pulse sequence generation should be possible in an integrated optic configuration by simply modifying the AWG structure shown in Fig. 4.2.

Fig. 4.8 shows a schematic representation of the suggested device, based on a modified AWG structure, which we have coined the DST-AWG [41]. By comparing this

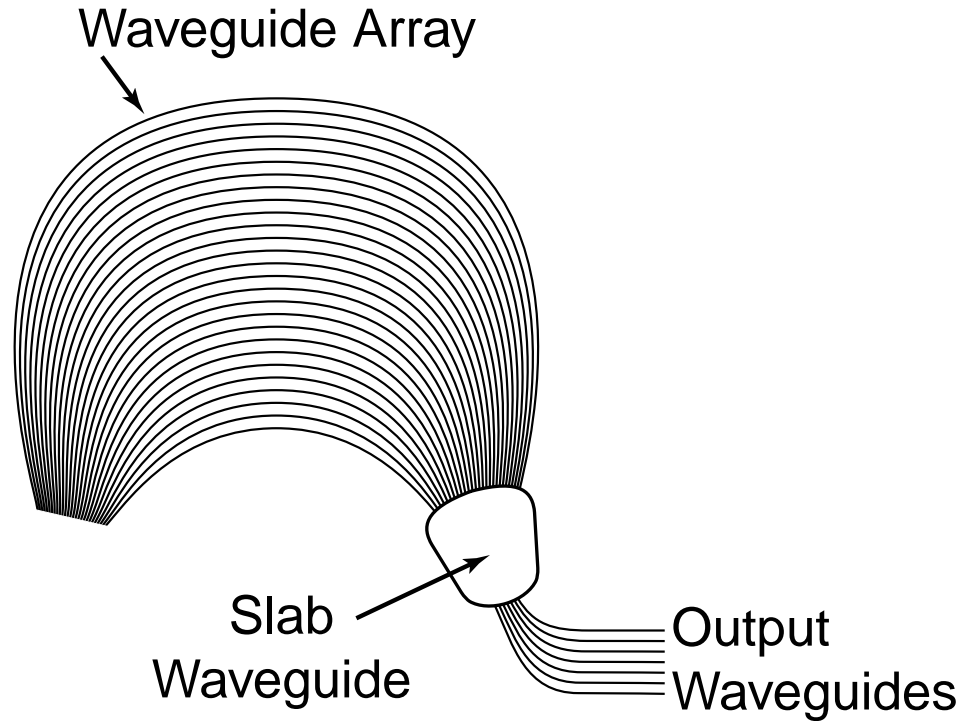


Fig. 4.8. DST-AWG device schematic.

structure to the standard AWG structure shown in Fig. 4.2, it is clear that the modifications consist of removing the input waveguide, and input slab waveguide of the standard AWG device. This modification permits direct access to the 'grating' of the integrated optic device so that an arbitrary spatial pattern may be imposed onto the waveguide array. The spatial pattern present at the input to the waveguide array should be mapped to the time domain on the output waveform in the same manner as the space-time mapping of the bulk optics DST pulse shaper discussed earlier.

A prototype request for this device was requested in a proposal to the Joint Optoelectronics Program (JOP) administered by the Optoelectronics Industry Development Association (OIDA) in September 1998. The JOP program is designed to facilitate exchange of prototype optoelectronic devices between users and suppliers in the United States and Japan. The charter of the JOP program mandates that the prototypes

must be non-catalog items (i.e. not commercially available), and must be for use in the development of "Computing Applications"; although, "Computing" is permitted to be quite broadly defined.

The DST-AWG prototype request was funded, using funds from NSF and DARPA valued at 2,400,000 Yen, in February 1999. However, due to administrative changes at OIDA, an official 'order' for the prototype was not placed with a Japanese vendor until April 2000. According to the information we have available, the prototype was scheduled to be delivered on September 18, 2000. Unfortunately, fabrication difficulties have delayed the delivery of the prototype, and as of this writing, OIDA has not been able to provide an updated delivery date. Initial experiments planned for this prototype, as well as potential for additional experiments will be discussed in the next chapter.

5. FUTURE DIRECTIONS

The significant body of work on DST pulse shaping, both in the bulk configuration and the integrated optic configuration, serves as a basis for substantially more work to be investigated in the future. Some aspects of new investigations are currently in progress while others need to be started; perhaps by new students with an interest in ultrafast technology.

The imaging components of the bulk optics configuration of the DST pulse shaping apparatus described in chapter 3 was indicated to be compatible with an optoelectronic modulator array so that the intensity of the individual pixelated spots could be modulated at high speed. While we do currently have an optoelectronic modulator array available for this purpose, to date it has not been successfully utilized in the pulse shaping apparatus. Clearly this is an experiment that should be completed in order to round out the body of work on the DST pulse shaper.

Currently there is work in progress within the Ultrafast Optics & Optical Fiber Communications Laboratory on the construction of a high repetition rate short pulse modelocked fiber laser. One target use of this laser, once operational, is to extend the bulk optics DST pulse shaping work to communications wavelengths. The current plan calls for the DST pulse shaper to be constructed utilizing a curved diffraction grating instead of the planar grating and lens described in chapter 3. Such a configuration, once

demonstrated, may increase interest in DST pulse shaping for communications applications as the inclusion of a curved grating simplifies the apparatus and could lead to implementing it, utilizing micro-optics, in a rather small package.

Concurrently, there is work underway to fabricate arrays of asymmetric Fabry-Perot modulators in the InP material system, in collaboration between Prof. Weiner's group, Prof. Melloch, and Prof. Ekmel Ozbay of Bilkent University in Turkey. These devices are of interest for use in the DST pulse shaper working in the 1.55 μm wavelength range. While the use of the currently available optoelectronic modulator array within the DST pulse shaper at 850 nm is of interest in terms of completeness, the InP based devices, once employed within the DST apparatus, have greater potential for interest within the optical communications industry.

Work on new implementation of the integrated optics devices based on AWG's is also in progress. As was stated in section 4.4, the first prototype DST-AWG device is expected to be delivered shortly. Experiments are expected to begin using this new device as soon as it arrives. Concurrently, we have been working with our collaborators at NTT Photonics Laboratories, on new implementations of the pulse train generation AWG devices. The next design, currently being fabricated at NTT, calls for tailoring the loss characteristics within the waveguide array of the AWG in order to produce an output pulse train consisting of approximately 21 pulses of equal amplitude. Initial indications are that the device appears to be functioning as designed, although it will not be tested with short pulses until it arrives at Purdue, and may be delivered in November of this year with experiments to start upon its arrival. Other potential device implementations are also under consideration.

As can be seen from the above descriptions of current, and planned experiments, there still is significant work to be completed related to the DST pulse shaping described here. The breadth and depth of projects requires significant resources both in terms of equipment as well as individuals to perform the work. Including myself, there are currently three students working on aspects of the above described projects. In order to continue making progress at a reasonable pace, at least this level of manpower commitment will need to be invested with perhaps one additional student.

LIST OF REFERENCES

- [1] A.M. Weiner, and J.P. Heritage, "Picosecond and femtosecond Fourier pulse shape synthesis," *Rev. Phys. Appl.*, **22**, 1619, (1987).
- [2] A.M. Weiner, J. P. Heritage, and E. M. Kirschner, "High-resolution femtosecond pulse shaping," *J. Opt. Soc. Amer. B* **5**, 1563-1572 (1988).
- [3] A.M. Weiner, "Femtosecond optical pulse shaping and processing," *Prog. Quantum Electron.* **19**, 161-238 (1995).
- [4] A.M. Weiner, D.E. Leaird, G.P. Wiederrecht, and K.A. Nelson, "Femtosecond pulse sequences used for optical control of molecular motion," *Science*, **247**, 1317 (1990).
- [5] A.M. Weiner, D.E. Leaird, D.H. Reitze, and E.G. Paek, "Femtosecond Spectral Holography," *IEEE J. Quantum Electron.*, **28**, 2251-2261 (1992).
- [6] A.M. Weiner, and S.-G. Park, "Prospects for ultrafast optical control of coherent charge oscillations in semiconductors. In W. H. Carter (Ed.), National Science Foundation (NSF) Forum on Optical Science and Engineering, **2524** (pp. 11-25). San Diego, CA: Proc. SPIE (1995).
- [7] A.M. Weiner, J.P. Heritage, R.J. Hawkins, R.N. Thurston, E.M. Kirschner, D.E. Leaird, and W.J. Tomlinson, "Experimental observation of the fundamental dark soliton in optical fibers," *Phys. Rev. Lett*, **61**, 2445 (1988).
- [8] A.M. Weiner, J.P. Heritage, and J.A. Salehi, "Encoding and decoding of femtosecond pulses," *Opt. Lett.*, **13**, 300-302 (1988).
- [9] A.M. Weiner, Y. Silberberg, H. Fouckhardt, D.E. Leaird, M.A. Saifi, M.J. Andrejco, and P.W. Smith, "Use of Femtosecond Square Pulses to Avoid Pulse Breakup in All-Optical Switching," *IEEE J. Quantum Electron*, **25**, 2648 (1989).
- [10] C.-C. Chang, H.P. Sardesai, and A.M. Weiner, "Code-division multiple-access encoding and decoding of femtosecond optical pulses over a 2.5-km fiber link," *IEEE Phot. Tech. Lett.*, **10**, 171-173 (1998).
- [11] A.M. Weiner, and D.E. Leaird, "Generation of Terahertz-Rate Trains of Femtosecond Pulses by Phase-only Filtering," *Opt. Lett.*, **15**, 51-53, (1990).

- [12] A.M. Weiner, D.E. Leaird, J.S. Patel, and J.R. Wullert, "Programmable Femtosecond Pulse Shaping by Using a Multielement Liquid Crystal Phase Modulator," *Opt. Lett.*, **15**, 326-328 (1990).
- [13] A.M. Weiner, D.E. Leaird, J.S. Patel, and J.R. Wullert, "Programmable shaping of femtosecond pulses by use of a 128-element liquid-crystal phase modulator," *IEEE J. Quantum Electron.*, **28**, 908-920, (1992).
- [14] M.A. Dugan, J.X. Tull, and W.S. Warren, "High-Resolution Acusto-Optic Shaping of Unamplified and Amplified Femtosecond Laser Pulses," *J. Opt. Soc. Am. B*, **14**, 2348-2358 (1997).
- [15] M. Haner, and W.S. Warren, "Synthesis of Crafted Optical Pulses by Time Domain Modulation in a Fiber-Grating Compressor," *Appl. Phys. Lett.*, **52**, 1458, (1988).
- [16] N.J. Halas, D. Krokell, and D. Grischkowsky, "Ultrafast light-controlled optical fiber modulator," *Appl. Phys. Lett.*, **50**, 886-888, (1988).
- [17] G. Imeshev, A. Galvanauskas, D. Harter, M.A. Arbore, M. Proctor, and M.M. Fejer, "Engineerable femtosecond pulse shaping by second-harmonic generation with Fourier synthetic quasi-phase-matching gratings," *Opt. Lett.*, **23**, 864-866, (1998).
- [18] D. Yelin, D. Meshulach, and Y. Silberberg, "Adaptive femtosecond pulse compression," *Opt. Lett.*, **22**, 1793-1795, (1997).
- [19] A. Efimov, and D.H. Reitze, "Programmable dispersion compensation and pulse shaping in a 26-fs chirped-pulse amplifier," *Opt. Lett.*, **23**, 1612-14, (1998).
- [20] Y. Ding, R.M. Brubaker, D.D. Nolte, M.R. Melloch, and A.M. Weiner, "Femtosecond pulse shaping by dynamic holograms in photorefractive multiple quantum wells," *Opt. Lett.*, **22**, 718-720, (1997).
- [21] T. Kurokawa, H. Tsuda, K. Okamoto, K. Naganuma, H. Takenouchi, Y. Inoue, and M. Ishii, "Time-space-conversion optical signal processing using arrayed-waveguide grating," *Elec. Lett.*, **33**, 1890-1891, (1997).
- [22] B. Colombeau, M. Vampouille, and C. Froehly, "Shaping of Short Laser Pulses by Passive Optical Fourier Techniques," *Opt. Comm.*, **19**, 201-204 (1976).
- [23] P. Emplit, J.P. Hamaide, F. Reynaud, C. Froehly, and A. Barthelemy, "Picosecond steps and dark pulses through nonlinear single mode fibers," *Opt. Commun.*, **62**, 374-379, (1987).
- [24] C. Froehly, B. Colombeau, and M. Vampouille, "Shaping and analysis of picosecond light pulses" in *Progress in Optics*, E. Wolf, Ed. **20**, 65 (1983).

- [25] C. Sauteret, M. Novaro, and O. Martin, "Passive pulse shaping by spectral narrowing of picosecond pulses," *Appl. Opt.*, **20**, 1487-1490, (1981).
- [26] P. Emplit, J.-P. Hamaide, and F. Reynaud, "Passive amplitude and phase picosecond pulse shaping," *Opt. Lett.*, **17**, 1358-1360 (1992).
- [27] P. Emplit, M. Haelterman, and J.-P. Hamaide, "Picosecond dark soliton over 1 km fiber at 850 nm," *Opt. Lett.*, **18**, 1047-1049, (1993).
- [28] D.E. Leaird, and A.M. Weiner, "Direct Space-to-Time Conversion for Ultrafast Optical Waveform Generation," in *Conference on Lasers and Electro-optics*, OSA Technical Digest (Optical Society of America, Washington DC), 99-100, (1998).
- [29] D.E. Leaird, and A.M. Weiner, "Ultrafast Optoelectronic Mux Apparatus," *Optical Society of America Annual Meeting 1998*, Baltimore, MD, 4-Oct-98 thru 9-Oct-98.
- [30] D.E. Leaird, and A.M. Weiner, "The Role of Lens-Slit Separation for Chirp Compensation in a Direct Space-to Time Femtosecond Pulse Shaper," *Ultrafast Optics and Optoelectronics*, Aspen, CO, 12-Apr-99 thru 16-Apr-99.
- [31] D.E. Leaird, and A.M. Weiner, "Chirp Compensation in a Femtosecond Direct Space-to-Time Optical Pulse Shaper," in *Conference on Lasers and Electro-optics*, OSA Technical Digest (Optical Society of America, Washington DC), 185-186, (1999).
- [32] D.E. Leaird, and A.M. Weiner, "Femtosecond Optical Packet Generation via a Direct Space-to-Time Pulse Shaper," *Opt. Lett.*, **24**, 853-855, (1999).
- [33] D.E. Leaird, and A.M. Weiner, "Chirp Characteristics and Multiwavelength Pulse Sequence Generation from a Direct Space-to-Time Pulse Shaper," *Gordon Conference on Nonlinear Optics & Lasers*, New London, NH, 25-Jul-99 thru 30-Jul-99.
- [34] D.E. Leaird, and A.M. Weiner, "500 GHz Wavelength-Division Multiplexed Pulse Train Generation from a Direct Space-to-Time Pulse Shaper," *Optical Society of America Annual Meeting*, Santa Clara, CA, 26-Sep-99 thru 30-Sep-99.
- [35] D.E. Leaird, and A.M. Weiner, "Generation of Femtosecond Optical Pulse Sequences from a Direct Space-to-Time Pulse Shaper," in *Ultrafast Optics and Optoelectronics 1999*, (Optical Society of America, Washington DC, 1999).
- [36] D.E. Leaird, and A.M. Weiner, "Wavelength tunable femtosecond pulse trains from a direct space-to-time pulse shaper," in *Conference on Lasers and Electro-Optics*, OSA Technical Digest (Optical Society of America, Washington DC), 410-411, (2000).

- [37] D.E. Leaird and A.M. Weiner, "Chirp control in the direct space-to-time pulse shaper," *Opt. Lett.*, **25**, 850-852 (2000).
- [38] D.E. Leaird, and A.M. Weiner, "Femtosecond direct space-to-time pulse shaping," submitted to *IEEE J. Quant. Elec.*
- [39] R. Adar, C.H. Henry, C. Dragone, R.C. Kistler, M.A. Milbrodt, "Broad-band array multiplexers made with silica wave-guides on silicon," *J. Lightwave Tech.*, **11**, 212-219, (1993).
- [40] K. Okamoto, "Recent progress of integrated optics planar lightwave circuits," *Opt. and Quant. Elec.* **31**, 107-129 (1999).
- [41] D.E. Leaird, and A.M. Weiner, "Ultrafast Space-to-Time Conversion for Computer Communications," a proposal submitted to Opto-electronic Industry Development Association (OIDA), (1998).
- [42] D.E. Leaird, and A.M. Weiner, "Direct space-to-time pulse shaper and optical pulse train generator," submitted to the United States Patent and Trademark Office (2000).
- [43] D.E. Leaird, S. Shen, A.M. Weiner, A. Sugita, S. Kamei, M. Ishii, and K. Okamoto, "1 THz Repetition Rate WDM Pulse Train Generation from an Arrayed-Waveguide Grating," in *Conference on Lasers and Electro-Optics Postdeadline Papers*, CPD18 (2000).
- [44] D.E. Leaird, S. Shen, A.M. Weiner, A. Sugita, S. Kamei, M. Ishii, and K. Okamoto, ">500 GHz repetition rate WDM pulse train generation via direct space-to-time pulse shaping – bulk & integrated optics implementations," invited to *IEEE LEOS Newsletter*.
- [45] D.E. Leaird, A.M. Weiner, S. Shen, A. Sugita, S. Kamei, M. Ishii, and K. Okamoto, "Generation of High Repetition Rate WDM Pulse Trains from an Arrayed-Waveguide Grating," submitted to *IEEE Photon. Tech. Lett.*
- [46] D.E. Leaird, S. Shen, A.M. Weiner, A. Sugita, S. Kamei, M. Ishii, and K. Okamoto, "High Repetition Rate Femtosecond WDM Pulse Generation using Direct Space-to-Time Pulse Shapers and Arrayed Waveguide Gratings," invited to *Opt. Quan. Elec.*
- [47] S. Kawanishi, H. Takara, K. Uchiyama, I. Shake, and K. Mori, "3Tbit/s (160 Gbit/s x 19 channel) optical TDM and WDM transmission experiment," *Electron. Lett.*, **35**, 826-827 (1999).
- [48] A.D. Ellis, J.K. Lucek, D. Pitcher, D.G. Moodie, and D. Cotter, "Full 10 x 10 Gbit/s OTDM data generation and demultiplexing using electroabsorption modulators," *Electron. Lett.*, **34**, 1766-1767 (1998).

- [49] O. Martinez, "Grating and prism compressors in the case of finite beam size," *J. Opt. Soc. Am. B*, **3**, 929-934, (1986).
- [50] M. Wefers, and K.A. Nelson, "Space-time profiles of shaped ultrafast optical waveforms," *IEEE J. Quant. Electron.*, **32**, 161-172, (1996).
- [51] J.W. Goodman, *Introduction to Fourier Optics* (McGraw-Hill, New York, 1968).
- [52] J.-C. Diels, and W. Rudolph, *Ultrashort Laser Pulse Phenomena* (Academic Press, San Diego, CA, 1996).
- [53] R.L. Morrison, S.L. Walker, and T.J. Cloonan, "Beam array generation and holographic interconnections in a free-space optical switching network," *Appl. Opt.*, **32**, 2512-2518 (1993).
- [54] A. Yariv, *Optical Electronics* (Saunders College Publishing, 1991).
- [55] J.T. Verdeyen, *Laser Electronics* (Prentice Hall, Englewood Cliffs, NJ, 1995).
- [56] S. Ramo, J.R. Whinnery, and T. Van Duzer, *Fields and Waves in Communications Electronics* (Wiley, 1994).
- [57] M.K. Smit, C. van Dam, "PHASAR-based WDM-devices: principles, design, and applications," *IEEE J. Sel. Top. Quant. Elec.*, **2**, 236-250 (1996).
- [58] C. Palmer, *Diffraction Grating Handbook*, 4th edition (Richardson Grating Lab, Rochester, NY, 2000).
- [59] I.Y. Khrushchev, J.D. Bainbridge, J.E.A. Whiteaway, I.H. White, and R.V. Petty, "Multiwavelength pulse source for OTDM/WDM applications based on arrayed waveguide grating," *IEEE Photon. Tech. Lett.*, **11**, 1659-1661 (1999).
- [60] T. Morioka, K. Uchiyama, S. Kawanishi, S. Suzuki, and M. Saruwatari, "Multiwavelength picosecond pulse source with low jitter and high optical frequency stability based on 200nm supercontinuum filtering," *Electron. Lett.*, **31**, 1064-1066 (1995).
- [61] H. Takahashi, K. Oda, H. Toba, and Y. Inoue, "Transmission characteristics of arrayed waveguide NxN wavelength multiplexer," *Journ. Light. Tech.*, **13**, 447-455 (1995).

APPENDIX

The diffraction analysis of section 3.3.2 was abbreviated for the readers' convenience. The complete derivation is included here. The starting place is equation (3.50) with the intermediate results of equations (3.47)-(3.51) substituted in:

$$\begin{aligned}
 E_5(x, \omega) = & \frac{1}{j\lambda d_2} \exp\left(\frac{-jk}{2d_2} x^2\right) \exp(-jkd_2) \\
 & \int dx_4 \exp\left(\frac{-jk}{2d_2} x_4^2\right) \exp\left(\frac{jk}{d_2} x x_4\right) \\
 & \exp\left(\frac{jk}{2f} x_4^2\right) \frac{1}{j\lambda d_1} \exp(-jkd_1) \exp\left(\frac{-jk}{2d_1} x_4^2\right) \\
 & \int dx_2 \exp\left(\frac{-jk}{2d_1} x_2^2\right) \exp\left(\frac{jk}{d_2} x_2 x_4\right) \\
 & s(\beta x_2) E_{in}(\omega) \exp(-j\gamma\omega x_2)
 \end{aligned} \tag{A.1}$$

Rearranging the order of the integrals produces the following

$$\begin{aligned}
 E_5(x, \omega) = & \frac{-1}{\lambda^2 d_1 d_2} \exp\left(\frac{-jk}{2d_2} x^2\right) \exp(-jkd_1) \exp(-jkd_2) E_{in}(\omega) \\
 & \int dx_2 s(\beta x_2) \exp(-j\gamma\omega x_2) \exp\left(\frac{-jk}{2d_1} x_2^2\right) \\
 & \int dx_4 \exp\left(\frac{-jk}{2d_1} x_2^2\right) \exp\left(\frac{jk}{d_2} x_2 x_4\right) \\
 & \exp\left(\frac{-jk}{2d_2} x_4^2\right) \exp\left(\frac{jk}{2f} x_4^2\right) \exp\left(\frac{jk}{d_2} x x_4\right)
 \end{aligned} \tag{A.2}$$

Then solve the second integral:

$$I = \int dx_4 \exp \left[\frac{-jk}{2} \left(\frac{1}{d_1} + \frac{1}{d_2} - \frac{1}{f} \right) x_4^2 \right] \exp \left[jk \left(\frac{x_2}{d_1} + \frac{x}{d_2} \right) \right] \quad (\text{A.3})$$

using eqn. (3.52) with the following substitutions.

$$\alpha = \frac{-k}{2} \left(\frac{1}{d_1} + \frac{1}{d_2} - \frac{1}{f} \right) = \frac{-k}{2} \left(\frac{d_2 f + d_1 f - d_1 d_2}{d_1 d_2 f} \right) \quad (\text{A.4})$$

and

$$\xi = k \left(\frac{x_2}{d_1} + \frac{x}{d_2} \right) \quad (\text{A.5})$$

The result is:

$$I = \sqrt{\frac{-j\lambda f d_1 d_2}{d_2 f + d_1 f - d_1 d_2}} \exp \left[\frac{jk}{2d_1} \left(\frac{d_2 f}{d_2 f + d_1 f - d_1 d_2} \right) x_2^2 \right] \exp \left[\frac{jk}{2d_2} \left(\frac{d_1 f}{d_2 f + d_1 f - d_1 d_2} \right) x^2 \right] \exp \left[jk \left(\frac{f}{d_2 f + d_1 f - d_1 d_2} \right) x_2 x \right] \quad (\text{A.6})$$

which is substituted back into eqn. (A.2) to yield:

$$E_5(x, \omega) = \frac{-1}{\lambda^2 d_1 d_2} \sqrt{\frac{-j\lambda f d_1 d_2}{d_2 f + d_1 f - d_1 d_2}} \exp[-jk(d_1 + d_2)] E_{in}(\omega) \exp \left[\frac{-jk}{2d_2} \left(\frac{d_2 f - d_1 d_2}{d_2 f + d_1 f - d_1 d_2} \right) x^2 \right] \int dx_2 s(\beta x_2) \exp(-j\gamma \omega x_2) \exp \left[\frac{-jk}{2d_1} \left(\frac{d_1 f - d_1 d_2}{d_2 f + d_1 f - d_1 d_2} \right) x_2^2 \right] \exp \left[jk \left(\frac{f}{d_2 f + d_1 f - d_1 d_2} \right) x_2 x \right] \quad (\text{A.7})$$

The spatial profile at the diffraction grating is then substituted in

$$s(x) = m(x) \exp \left(\frac{-x^2}{w^2} \right) \exp \left(\frac{-jk}{2R} x^2 \right) \quad (\text{A.8})$$

along with the change of variable:

$$x' = \beta x_2 \rightarrow dx_2 = \frac{1}{\beta} dx' \quad (\text{A.9})$$

to yield the following

$$\begin{aligned} E_5(x, \omega) = & \frac{-1}{\lambda^2 d_1 d_2} \sqrt{\frac{-j\lambda f d_1 d_2}{d_2 f + d_1 f - d_1 d_2}} \exp[-jk(d_1 + d_2)] E_{in}(\omega) \\ & \exp\left[\frac{-jk}{2d_2} \left(\frac{d_2 f - d_1 d_2}{d_2 f + d_1 f - d_1 d_2}\right) x^2\right] \int dx' \frac{1}{\beta} m(x') \exp\left(\frac{-x'^2}{w^2}\right) \\ & \exp\left(\frac{-j\gamma\omega}{\beta} x'\right) \exp\left[\frac{-jk}{2} \left(\frac{1}{R} + \frac{f - d_2}{\beta^2 (d_2 f + d_1 f - d_1 d_2)}\right) x'^2\right] \\ & \exp\left[jk \left(\frac{f}{\beta (d_2 f + d_1 f - d_1 d_2)}\right) x' x\right] \end{aligned} \quad (\text{A.10})$$

The integral above may be recognized as a Fourier transform by collecting terms

$$\begin{aligned} Z(x) = & \frac{-1}{\lambda^2 d_1 d_2} \sqrt{\frac{-j\lambda f d_1 d_2}{d_2 f + d_1 f - d_1 d_2}} \exp[-jk(d_1 + d_2)] \\ & \exp\left[\frac{-jk}{2} \left(\frac{f - d_1}{d_2 f + d_1 f - d_1 d_2}\right) x^2\right] \end{aligned} \quad (\text{A.11})$$

$$s'(x') = m(x') \exp\left(\frac{-x'^2}{w^2}\right) \exp\left[\frac{-jk}{2} \left(\frac{1}{R} + \frac{f - d_2}{\beta^2 (d_2 f + d_1 f - d_1 d_2)}\right) x'^2\right] \quad (\text{A.12})$$

$$K = \frac{k f}{d_2 f + d_1 f - d_1 d_2} \quad (\text{A.13})$$

to cast (A.10) in the following form:

$$E_5(x, \omega) = Z(x) \frac{1}{\beta} E_{in}(\omega) \int dx' s'(x') \exp\left(\frac{-j\gamma\omega}{\beta} x'\right) \exp\left(\frac{jK}{\beta} x' x\right) \quad (\text{A.14})$$

Performing the integral yields the spectrum before the output slit:

$$E_5(x, \omega) = Z(x) \frac{\sqrt{2\pi}}{\beta} E_{in}(\omega) S'\left(\frac{Kx}{\beta} - \frac{\gamma\omega}{\beta}\right) \quad (\text{A.15})$$

with the corresponding output field given by the Fourier transform of (A.15):

$$e_s(x, t) = \mathbb{Z}(x) \frac{1}{\beta} \int d\omega E_{in}(\omega) S' \left[\frac{-\gamma}{\beta} \left(\omega - \frac{Kx}{\gamma} \right) \right] \quad (\text{A.16})$$

or

$$e_s(x, t) = \frac{\mathbb{Z}(x)}{\gamma} e_{in}(t) * s' \left(\frac{-\beta}{\gamma} t \right) \exp \left(\frac{jKx}{\gamma} t \right) \quad (\text{A.17})$$

The effect of the output slit can be handled either by assuming an ideal (delta function) slit as was done in section 3.3.2 (diffraction analysis) and 3.4.1 (multiple output channels), or a general slit function as was done in section 3.2.3 (temporal window).

VITA

Daniel E. Leaird
137 Ivy Hill Drive
West Lafayette, IN 47906
(765) 497-9795
leaird@purdue.edu

Work Experience

- **Research Engineer**, Purdue University, West Lafayette, IN, 3/96 to present. Conduct research projects in the area of ultrafast pulse shaping and applications of high speed optoelectronic modulator arrays. Assist group members in diagnosing problems with research systems. Operate and maintain the Ultrafast Optics & Optical Fiber Communications Laboratory. Laboratory automation system design and implementation. Advisor/mentor for undergraduate research assistants.
- **Research Assistant**, Purdue University, West Lafayette, IN, 6/94 to 3/96. Conduct research projects in the area of ultrafast optics. Advisor/mentor for undergraduate research assistants.
- **Teaching Assistant**, Purdue University, West Lafayette, IN, 8/94 to 5/95. Assist students through two different courses - a sophomore level circuits lab and a senior level fiber optics lab. Plan lectures, create quizzes, grade laboratory reports, supervise two undergraduate assistants.
- **Member of Technical Staff**, Bellcore, Red Bank, NJ, 6/87 to 6/94. Initial role as a laboratory technician progressing to the level of lab manager. Projects responsibilities in four diverse areas: optics research, computer systems administration, ISDN application development, and technology assessment.
 - ⇒ Daily operation and maintenance of a state-of-the-art femtosecond laser laboratory. Co-investigator on forward looking research experiments on subjects related to optical fiber communication technology. Computer data acquisition system design and implementation on various hardware platforms including interfacing to an array of laboratory instrumentation. Data analysis and presentation.
 - ⇒ Supervise summer interns, mentor for new employees.
- **Senior Staff Technologist**, Bellcore, Morristown, NJ, 6/86 to 8/86. 10-week internship to design and construct a computer driven optical auto-correlation apparatus for pulse width measurements of a modelocked external cavity diode laser to be used in clock recovery experiments.

Patent Activity

Direct Space-to-Time Pulse Shaper and Optical Pulse Train Generator, D.E. Leaird and A.M. Weiner, United States patent filed by Purdue University Research Foundation 22-Sep-00.

Education

Purdue University, School of Electrical and Computer Engineering, West Lafayette, IN, 12/96 to present. Ph.D. program studying femtosecond pulse processing. Degree expected 12/2000.

Purdue University, School of Electrical and Computer Engineering, West Lafayette, IN, 6/94 to 12/96. Master of Science. Thesis entitled 'Characterization of Asymmetric Fabry-Perot Reflection Modulators at 1.55 microns Using a Tunable CW Erbium Fiber Laser'.

Ball State University, Muncie, IN, 9/83 to 6/87. Bachelor of Science. Physics major, Mathematics and Computer Science minors.

Honors

New Focus Student Award, Optical Society of America Annual Meeting, 9/99.

Magoon Award, 5/95: Outstanding performance of Teaching Assistant duties.

Bellcore Team Awards, 94/95: In recognition of project team accomplishments. Three separate awards.

Bellcore Award of Excellence, 1988.

American Institute of Physics Industrial Intern Program, 4/86.

Professional Organizations

Optical Society of America. 1989 to present.

Personal&Activities

Married 13 years (Jennifer), three children – Ian (8), Maclaine (5), and Aidan (3).

Advisor & Treasurer, Purdue Goju Ryu Karate Club, 5/96 to present.

Line Officer, Atlantic Highlands First-Aid & Safety Squad, 1991 & 92.

Bellcore Emergency Response Team member, 8/87 to 6/94.

Volunteer Emergency Medical Technician, Firefighter, CPR Instructor, 12/88 to 6/94.